Range Geolocation Accuracy of C-/L-Band SAR and Its Implications for Operational Stack Coregistration

Zhang Yunjun, Heresh Fattahi, *Member, IEEE*, Xiaoqing Pi, Paul Rosen, *Fellow, IEEE*, Mark Simons, *Senior Member, IEEE*, Piyush Agram, and Yosuke Aoki, *Member, IEEE*

***Abstract*— Time series analysis of synthetic aperture radar (SAR) and interferometric SAR generally starts with coregistration for the precise alignment of the stack of images. Here, we introduce a model-adjusted geometrical image coregistration (MAGIC) algorithm for stack coregistration. This algorithm corrects for atmospheric propagation delays and known surface motions using existing models and ensures simplicity and computational efficiency in the data processing systems. We validate this approach by evaluating the impact of different geolocation errors on stacks of the C-band Sentinel-1 and L-band ALOS-2 data, with a focus on the ionosphere. Our results show that the impact of the ionosphere dominates Sentinel-1 ascending (dusk-side) orbit and ALOS-2 data. After correcting for ionosphere using the JPL high-resolution global ionospheric maps, with topside total electron content (TEC) estimated from GPS receivers onboard the Sentinel-1 platforms, solid Earth tides, and troposphere, the mis-registration RMSE reduces by over a factor of four from 0.20 to 0.05 m for Sentinel-1 and from 2.66 to 0.56 m for ALOS-2. The results demonstrate that for Sentinel-1, the MAGIC approach is accurate enough in the range direction for most applications, including interferometry; while for the L-band SAR, it can be potentially accurate enough if topside TEC is available. Based on our current understanding of different error sources, we evaluate the expected range geolocation error budget for the upcoming NISAR mission with an upper bound of the relative geolocation error of 1.3 and 0.2 m for its L- and S-band SAR, respectively.**

***Index Terms*— Big-data, coregistration, geodesy, geolocation, interferometric SAR (InSAR), ionosphere, solid Earth tides, synthetic aperture radar (SAR), time series analysis.**

NOMENCLATURE

CLR	CODE low-resolution (GIM).
CODE	Center for orbit determination in Europe.
DEM	Digital elevation model.
EIA	Equatorial ionization anomaly.
ERA5	ECMWF re-analysis version 5.
ETAD	Extended timing annotation dataset.
GIM	Global ionospheric maps.
GNSS	Global navigation satellite system.
GPS	Global positioning system.
InSAR	Interferometric SAR.
IPP	Ionospheric piercing point.
IW	Interferometric wide (swath mode).
JHR	JPL high-resolution (GIM).
JLR	JPL low-resolution (GIM).
JPL	Jet Propulsion Laboratory.
LOS	Line of sight.
MAD	Median absolute deviation.
MAGIC	Model-adjusted geometrical image coregistration.
NISAR	NASA–ISRO SAR.
OTL	Ocean tidal loading.
RMSE	Root-mean-square error.
S1	Sentinel-1.
SAR	Synthetic aperture radar.
SET	Solid Earth tides.
SLC	Single look complex.
STD	Standard deviation.
SWOT	Surface water and ocean topography.
TEC	Total electron content.
TECU	TEC unit.
TPP	Topside IPP.
UTC	Universal time coordinated.

Manuscript received January 11, 2022; revised March 18, 2022; accepted April 5, 2022. Date of publication April 18, 2022; date of current version May 9, 2022. This work was supported by the Jet Propulsion Laboratory Advanced Concept, the NASA–ISRO SAR (NISAR) and the Observational Products for End-users from Remote sensing Analysis (OPERA) projects. *(Corresponding author: Zhang Yunjun.)*

Zhang Yunjun, Mark Simons, and Piyush Agram are with the Seismological Laboratory, Division of Geological and Planetary Sciences, California Institute of Technology, Pasadena, CA 91125 USA (e-mail: zyunjun@caltech.edu).

Heresh Fattahi, Xiaoqing Pi, and Paul Rosen are with the Jet Propulsion Laboratory, California Institute of Technology, Pasadena, CA 91109 USA.

Yosuke Aoki is with the Earthquake Research Institute, The University of Tokyo, Tokyo 113-0032, Japan.

Digital Object Identifier 10.1109/TGRS.2022.3168509

I. INTRODUCTION

TIME series analysis of SAR and InSAR have shown to be powerful imaging techniques to better understand the Earth system via mapping and measuring changes in the cryosphere, ecosystem, hydrology, and solid Earth deformation [1]–[4]. In general, the first step of time series analysis is the precise alignment of a stack of SAR images known as coregistration. In the early 1990s, standard image registration procedures, such as affine transformation with parameters estimated from empirical methods, were used to account for distortion effects caused by the different imaging geometries [5]. A sufficient number of tie points distributed all over the images

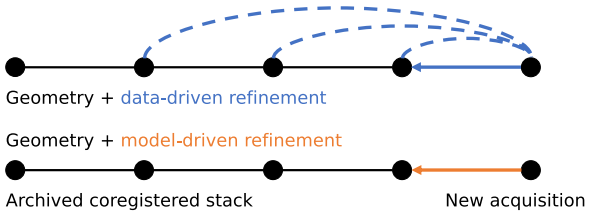

Fig. 1. Updating strategies for the stack coregistration of SAR big-data. Solid arrows represent the mis-registration refinement of the new acquisition. Dashed lines represent the redundant pairs of data-driven mis-registrations used to estimate the refinement of the new acquisition.

are usually required to precisely estimate the transformation parameters. Since the late 2000s, geometrical coregistration based on the precise orbit and external DEM, refined by data-driven mis-registrations [6], has been used to leverage the inherently good geolocation accuracy of SAR systems [7]. This approach requires fewer tie points, thus reducing the dependency of coregistration on data quality and operational modes [6].

The mis-registration between two SAR images is usually estimated empirically using cross-correlation or spectral diversity techniques [8]–[10]. For a stack of SAR images, a network-based approach can be adapted to estimate the mis-registration time series [11], [12]. With the ever-growing volume of SAR data, high demands for the operational time series analysis, and near real-time update of existing time series, it is of interest to evaluate the feasibility of using external models and products to predict the refinement, instead of using the data-driven refinement, for operational stack coregistration. We call this the model-adjusted geometrical image coregistration (MAGIC) approach.

The MAGIC approach has the following advantages. First, it is computationally less expensive to calculate the mis-registration refinement from external models and products than to estimate empirically using cross-correlation or spectral diversity techniques. Second, the model-driven refinement calculation is independent for each acquisition, thus adding a new acquisition to the stack does not require processing the previously archived coregistered images, resulting in a simpler data system (Fig. 1). Third, the MAGIC approach does not require tie points, thus, is applicable to land areas with low coherence and to oceanic applications. Less processing needs and a simpler data system are desirable for an operational data system and big-data processing.

Mis-registration is driven mainly by errors in the SAR platform's state vector (orbital error), timing errors in the SAR instrument, atmospheric propagation delays, motions of the Earth's surface due to tidal and loading effects, and DEM errors. Current spaceborne SAR missions such as Sentinel-1 have geometric design and control with orbit determination accuracy down to the centimeter level [13]. The impact of atmospheric delays, tidal forces, and systematic SAR processing effects have been evaluated for the X-band and C-band SAR [14]–[16]. However, the impact of ionospheric delay on the geolocation of the L-band SAR has not been fully understood.

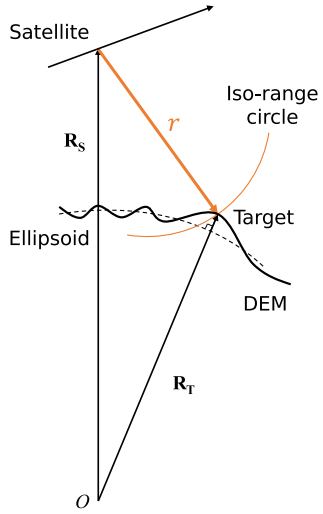

Fig. 2. Geometry of the Doppler centroid plane for SAR geolocation. $\mathbf{R_S}$ is the position vector of the SAR platform. $\mathbf{R_T}$ is the position vector of the target on the ground. r is the slant range distance.

Here, we investigate geolocation errors in the range direction with a focus on the ionospheric effect for the low-frequency (i.e., L-band and S-band) SAR and its correction methods. In particular, we evaluate the performance of the GIM using Sentinel-1 and ALOS-2 data and explore the correction for the topside ionosphere above the Sentinel-1's orbit for geolocation error correction purposes. Together with corrections for the troposphere and solid Earth tides (SET), we evaluate the feasibility of operational geometrical stack coregistration for time series applications, including interferometry.

In what follows, we first briefly review the theory of SAR geolocation (Section II) and associated error sources (Section III). The detailed ionospheric delay calculation is presented in Section IV. We then use SAR offset time series (Section V) as observations to compare with the prediction of the model-driven refinement in the real-data experiments (Section VI), followed by a discussion of results (Section VII) and conclusions (Section VIII).

II. SAR Geolocation Theory

For an imaging radar, the location of an arbitrary pixel is determined by the intersection of the centroid of the radar beam with the ground surface [7]. In a geocentric-Cartesian coordinate system (Fig. 2), this intersection can be described by the range-Doppler equation as

$$\frac{2\mathbf{V_S}(t)\cdot(\mathbf{R_T}-\mathbf{R_S}(t))}{\lambda\cdot r} = f_{\mathrm{DC}}(t,r) \tag{1}$$

$$|\mathbf{R_T}-\mathbf{R_S}(t)| = r \tag{2}$$

where λ is the radar wavelength, $f_{\mathrm{DC}}(t,r)$ is the Doppler centroid of the target at azimuth time (slow time) t and slant range (fast time) r, and $\mathbf{V_S}(t)$ and $\mathbf{R_S}(t)$ are the velocity and position vector of the sensor at azimuth time t, respectively. $\mathbf{R_T} = (x_T, y_T, h(x_T, y_T))$ is the position vector of the corresponding ground target where h is the height interpolated from DEM at the horizontal coordinates (x_T, y_T).

Given the precise obit of the SAR platform and a DEM, one can analytically relate the radar coordinates (t, r) to the geographic coordinates $(x_T, y_T, h(x_T, y_T))$ based on equations (1) and (2). We refer to forward mapping as the process to map the radar coordinates to the geographic coordinates and inverse mapping as the process to map the geographic coordinates back to the radar coordinates. Since the system of equations is nonlinear, one can start with an initial guess of the solution and iterate until convergence. The iterative search algorithm, such as Newton–Raphson, can be used to obtain the optimized solution. Detailed algorithms can be found in Sansosti *et al.* [6] and Eineder [17]. The two processes are commonly used for geometrical coregistration and geocoding.

For geometrical coregistration, the procedure includes forward mapping of the first image, followed by inverse mapping of the outputs of the previous step to the orbit of the second image [18]. An alternative procedure is to apply inverse mapping from an existing DEM to the orbits of both SAR images to compute their radar coordinates, which are then used to pull chips from the observed SAR images for the offset estimation [19], [20]. Mapping the radar data and products into a geographic coordinate system is known as geocoding. This process commonly involves inverse mapping the geographic coordinates of the desired geocoded cells to the radar coordinates, then interpolating or multilooking [21] the data in the radar coordinates for the desired pixel and assigning the interpolated value to the geocoded cell. Inverse mapping can be also used in the time-domain SAR focusing algorithms for backprojection [22], such as the recently introduced geocoded SLC [23], [24]. The accuracy of geometrical coregistration depends on the relative geolocation accuracy between SAR images while the geocoding accuracy depends on the absolute geolocation accuracy of the SAR data.

III. Sources of SAR Range Geolocation Errors

We review here the impact of the atmospheric propagation delay and motions of the Earth's surface on the SAR geolocation accuracy in the range direction.

A. Overview of Atmospheric Propagation Delay

As the radar signal travels through Earth's atmosphere, the refractive index n introduces a propagation delay. This delay is the difference between the physical path of the signal propagation through the atmosphere r and the geometrical path between the source of the signal (radar antenna's phase center) and the target on the ground r_o. Following Fermat's principle, the single-path atmospheric delay can be expressed as [25]

$$r_{\text{atm}} = \int n dr - \int dr_0 = \int N dr + \left(\int dr - \int dr_0 \right) \quad (3)$$

where $N = n - 1$ is the refractivity. On the right-hand side, the first term represents the atmospheric delay and the second term represents the bending of the microwave signal through the atmosphere. For elevation angles $\geq 5°$, i.e., incidence angle $\leq 85°$, the bending effect is commonly ignored [26].

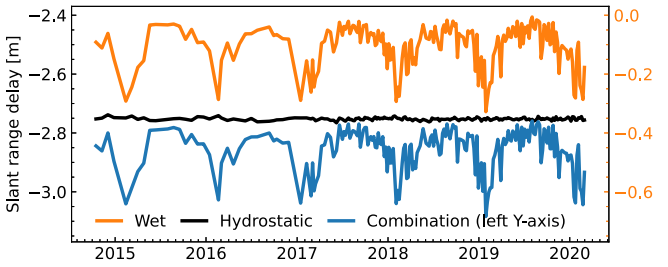

Fig. 3. Single-path absolute tropospheric delay time series in LOS direction at the acquisition time for Sentinel-1 descending track 156 at [S21.29°, W69.22°] in Chile using ERA5. Orange, black, and blue lines present contributions from the wet air, dry air (hydrostatic), and the combination of both, respectively. The denser sampling from September 2016 onward is due to the addition of Sentinel-1B.

B. Ionospheric Propagation Delay

At altitudes above ~50 km, radiation (mainly from the Sun) ionizes atmospheric atoms and molecules forming the ionosphere. Refractivity in the ionosphere is mainly controlled by the number of free electrons. Due to the dispersive nature of the ionosphere with respect to the microwave signal, the propagation of the microwave signal traveling through the ionosphere results in a group delay and a phase advance. They are equal in magnitude but opposite in sign. The group delay is of interest for geolocation. Detailed calculation of the ionospheric delay is described in Section IV.

C. Tropospheric Propagation Delay

At altitudes up to ~30 km, which forms the troposphere, refractivity is mainly controlled by temperature, water vapor, and dry air partial pressure [27]. All of these parameters are available from the global atmospheric models, such as the ERA5 global atmospheric reanalysis dataset from the European Centre for Medium-Range Weather Forecasts (ECMWF), Reading, U.K. [28]. The total zenith tropospheric delay can be integrated and mapped to the radar line-of-sight (LOS) direction using the PyAPS software [29]. ERA5 has a latency of five days for the rapid solution and approximately three months for the final solution. One could also use the high-resolution ECMWF numerical weather model (HRES), which has a latency of 5–10 hours.[1]

The zenith hydrostatic delay is ~2.3 m at sea level at typical meteorological conditions, while the zenith wet delay varies from a few mm at the polar region to ~40 cm at the equatorial region [25]. The hydrostatic delay dominates the overall magnitude (the absolute geolocation error), while the wet delay dominates the temporal variation (the relative geolocation error), as shown in Fig. 3, for the Sentinel-1 descending dataset in Chile from Section VI.

D. Overview of Earth Motions

The motion of the Earth's surface is driven by the gravitational pull from the Sun and the Moon (solid Earth tides), the change of the rotational axis (pole tides), the loading

[1] https://www.ecmwf.int/en/forecasts/datasets/set-i

effects from the ocean tides (OTL), the atmospheric and hydrological loading [14] and the surface deformation, such as those induced by tectonic, volcanic, glacial, and anthropogenic processes. Displacements from tidal and loading effects are periodic with different time scales and amplitudes. SET often reaches 40 and 10 cm in vertical and horizontal directions, respectively [30]. OTL could reach up to 10 cm in the coastal region and less than 1 cm in the inner continental region [30]–[32]. Surface deformation from tectonic and nontectonic processes has a wide range: from a few mm/year of interseismic deformation to up to several km/year of glacier movement. Contributions from the rest (pole tides, atmospheric loading and hydrological loading) are secondary. Pole tides could reach up to 2.5 and 0.7 cm in vertical and horizontal directions [30]. Atmospheric loading has the largest amplitude in the inner continental region and could reach up to 0.5 cm and less than 0.1 cm in vertical and horizontal directions [33]. Hydrological loading has typical values of a few millimeters and could reach up to 2 cm [34].

E. Solid Earth Tides

Following the 2010 International Earth Rotation and Reference Systems Service (IERS) conventions, the SET displacement in the east, north, and up directions ($r^e_{\mathrm{SET}}, r^n_{\mathrm{SET}}, r^u_{\mathrm{SET}}$) can be calculated with an accuracy of less than 1 mm [30], then projected to the radar LOS direction as

$$\begin{aligned} r_{\mathrm{SET}} = & -r^e_{\mathrm{SET}} \sin(\theta) \sin(\beta) \\ & + r^n_{\mathrm{SET}} \sin(\theta) \cos(\beta) \\ & + r^u_{\mathrm{SET}} \cos(\theta) \end{aligned} \tag{4}$$

where θ and β are the incidence angle and azimuth angle of the LOS vector on the ground. In this article, we use the *solid* program [35] with a Python wrapper, named PySolid[2] for the SET calculation.

1) Frequency Aliasing: Fig. 4 shows an example time series of r_{SET} and its power spectral density. SET is dominated by the principal lunar semidiurnal M_2 tide, with a period of 12.4206 hours. With the typical re-visit time of several days, the SAR instrument would undersample the M_2 tide causing frequency aliasing. This aliasing phenomenon applies to both SET [36] and OTL [31] in SAR and InSAR observations. The alias frequency f_a can be calculated as

$$f_a = |f - f_s \cdot \mathrm{round}(f/f_s)| \tag{5}$$

where f is the signal frequency, f_s is the sampling frequency, and $round$ is the nearest integer operator. With a sampling interval of 12 days, such as Sentinel-1 and NISAR, the alias frequency for the M_2 tide would be 64.1 days [blue dots in Fig. 4(a)]. Thus, we would expect a periodic displacement contribution with 5.7 cycles per year in SAR absolute range change time series, which is what we observed from the Sentinel-1 data in Chile in Section VI-A.

[2]Available on GitHub at https://github.com/insarlab/PySolid

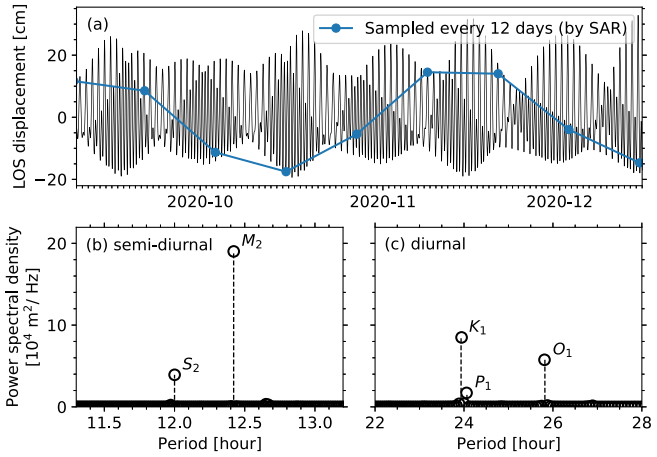

Fig. 4. Solid Earth tides at Los Angeles, CA, USA at [N34°, W118°]. (a) LOS displacement time series assuming an incidence angle of 42° and an azimuth angle of 100°. Blue dots represent displacement sampled by SAR sensor with a re-visit time of 12 days. (b) and (c) Power spectral density of (a) in the semidiurnal and diurnal frequency ranges, respectively. K_1, M_2, O_1, P_1, and S_2 are the Darwin symbol of the tidal constituents.

2) Along Track Acquisition Time Variation for SAR: Solid Earth tides vary slowly in space but fast in time. The fast temporal variation could lead to a spatial gradient due to the acquisition time difference within one SAR image as the satellite moves along the orbit, especially for long data tracks, in addition to the spatial gradient caused by the variation of incidence angle [36] and azimuth angle from the SAR imaging geometry. In Los Angeles, for example (Fig. 4), the maximum LOS SET displacement rate is 1.9 mm/min. With the typical SAR satellite speed on the ground of 6.8 km/s, the acquisition time variation would result in a gradient up to 0.5 mm per 100 km in the along-track direction in the SAR range offset or InSAR phase, if it is not accounted for.

IV. Ionospheric Range Delay From GNSS-Based Total Electron Content

Under the first-order assumption of ionospheric effect, which accounts for more than 99.9% of the refractivity for the L-band and even more for higher frequencies, the single-path absolute ionospheric delay in the LOS direction can be expressed as [30]

$$r_{\mathrm{iono}} = \mathrm{TEC} \cdot K / f_0^2 \tag{6}$$

where $K = 40.31\,\mathrm{m}^3 \cdot \mathrm{s}^{-2}$ is a constant, f_0 is the radar carrier frequency in Hz, and TEC is the number of free electrons in a tube of $1\,\mathrm{m}^2$ cross section along the slant range in the radar LOS direction from the ground to the SAR platform.

A. Ionospheric Mapping Function

The dual-frequency observations of global navigation satellite system (GNSS) allow to estimate global maps of vertical TEC (VTEC) [37]. The VTEC products can be used to evaluate and correct for the impact of ionosphere on SAR geolocation [14]. We map the radar LOS geometry from the ground to the ionospheric altitude by adopting the widely used thin-shell assumption of the effective ionosphere layer, as shown in Figs. 5 and 6. We calculate TEC from VTEC at

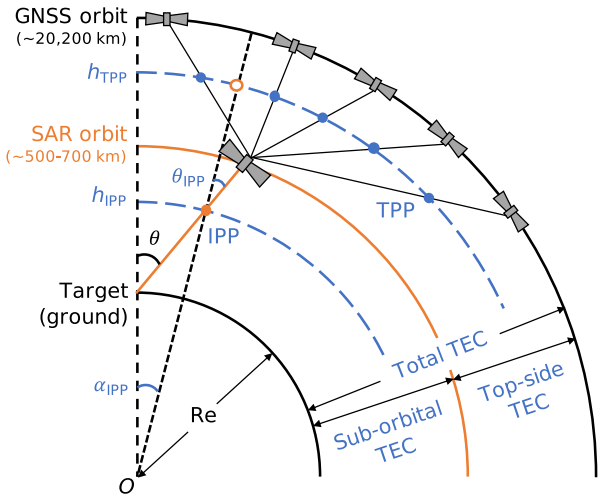

Fig. 5. Mapping geometry of GNSS-based TEC products. Re is the Earth radius, IPP for ionospheric piercing point, and TPP for topside ionospheric piercing point. θ and θ_{IPP} are the incidence angle of the radar LOS vector on the ground and at IPP, respectively. α_{IPP} is the geocentric angle distance between the target and IPP.

the IPP, i.e., the intersection point of the radar LOS vector with the thin-shell ionosphere in (ρ_{IPP}, ϕ_{IPP}) as

$$\mathrm{TEC} = \frac{\mathrm{VTEC}(\rho_{IPP}, \phi_{IPP})}{\cos(\eta_{IPP})} \tag{7}$$

where ρ and ϕ represent the latitude and longitude, respectively; η_{IPP} is the refraction angle of the LOS vector at IPP. η_{IPP} can be calculated from the incidence angle at IPP θ_{IPP} following Snell's law as

$$\eta_{IPP} = \arcsin\left(\frac{n_0}{n_{iono}}\sin(\theta_{IPP})\right) \tag{8}$$

where $n_0 = 1$ is the refractive index of vacuum and n_{iono} is the group refractive index of ionosphere. n_{iono} is a function of the electron density and frequency of interest and can be calculated to the first order from VTEC as [25]

$$n_{iono} = 1 + \mathrm{VTEC}(\rho_{IPP}, \phi_{IPP}) \cdot K / f_0^2. \tag{9}$$

The ionospheric sensitivity can be summarized from equation (6)–(9) as a nonlinear function of the vertical TEC as

$$\begin{cases} r_{iono} = a \Big/ \cos\left[\arcsin\left(\dfrac{\sin(\theta_{IPP})}{1+a}\right)\right] \\ a = \mathrm{VTEC}(\rho_{IPP}, \phi_{IPP}) \cdot K / f_0^2. \end{cases} \tag{10}$$

Assuming a spherical coordinate system, θ_{IPP} can be calculated from θ (the incidence angle of the LOS vector on the ground) as

$$\theta_{IPP} = \arcsin\left(\frac{\mathrm{Re}\cdot\sin(\theta)}{\mathrm{Re}+h_{IPP}}\right) \tag{11}$$

where Re is the Earth radius, and h_{IPP} is the effective height of the ionosphere, which is commonly set to 450 km [38].

Given the position of the target on the ground (ρ_T, ϕ_T), the IPP position (ρ_{IPP}, ϕ_{IPP}) can be calculated following the spherical distance formula as

$$\begin{cases} \rho_{IPP} = \arcsin[\sin(\rho_T)\cos(\alpha_{IPP}) \\ \qquad\qquad + \cos(\rho_T)\sin(\alpha_{IPP})\cos(\beta)] \\ \Delta\phi = \mathrm{atan2}[-\sin(\alpha_{IPP})\cos(\rho_T)\sin(\beta), \\ \qquad\qquad \cos(\alpha_{IPP}) - \sin(\rho_T)\sin(\rho_{IPP})] \\ \phi_{IPP} = \mathrm{mod}(\phi_T + \Delta\phi + \pi, 2\pi) - \pi \end{cases} \tag{12}$$

where $\alpha_{IPP} = \theta - \theta_{IPP}$ is the geocentric angular distance between the target and IPP, β is the azimuth angle of the LOS vector from target to SAR platform measured from the north with anticlockwise as positive. Note that the spherical formula ignores the ellipsoidal effects and could give errors up to 0.0055°, which is negligible for locating the much coarser resolution GNSS-based VTEC products. Nevertheless, one could use the more accurate geodetic formula instead.

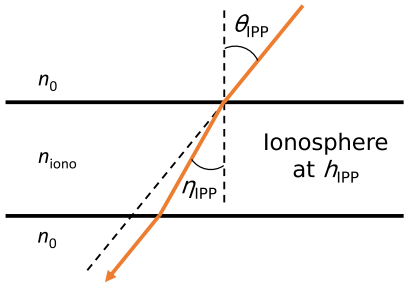

Fig. 6. Refraction geometry of microwave signal traveling through the ionospheric layer with refractive index of n_{iono}. n_0 is the refractive index of the vacuum. θ_{IPP} and η_{IPP} are the incidence and refraction angle of the radar LOS vector at IPP, respectively.

B. Characteristics of Ionospheric Range Delay

We examine the characteristics of the ionospheric range delay as a function of the vertical TEC for different radar frequencies at the L- (1.257 GHz, NISAR), S- (3.2 GHz, NISAR), C- (5.405 GHz, Sentinel-1), and X- (9.65 GHz, TerraSAR-X) bands. Calculations are based on equation (6)–(11) assuming an incidence angle of 42° for the LOS vector on the ground.

1) Ionospheric Impact on Geocoding: Fig. 7(a) shows the ionospheric delay for different radar frequencies. A vertical TEC of 20 TECU, which is commonly seen, causes a range delay of 5.1 m at the L-band. The same amount of TEC causes significantly less delay of 0.8, 0.3, and 0.1 m in the S-, C-, and X-bands, respectively.

2) Ionospheric Impact on Geometrical Coregistration: Fig. 7(a) right-hand side shows the ionospheric range delay in units of slant range spacing for different range bandwidths. A vertical TEC difference of 20 TECU between two SAR acquisitions results in 0.8, 1.5, and 2.7 pixels of range mis-registration at the L-band for range bandwidths of 24, 44, and 80 MHz, respectively. The same amount of ionosphere variation results in mis-registrations of 0.42, 0.14, and 0.08 pixels at the S-, C-, and X-bands with range bandwidths of 75 (NISAR), 64.35 (Sentinel-1), and 109.89 MHz (TerraSAR-X), respectively.

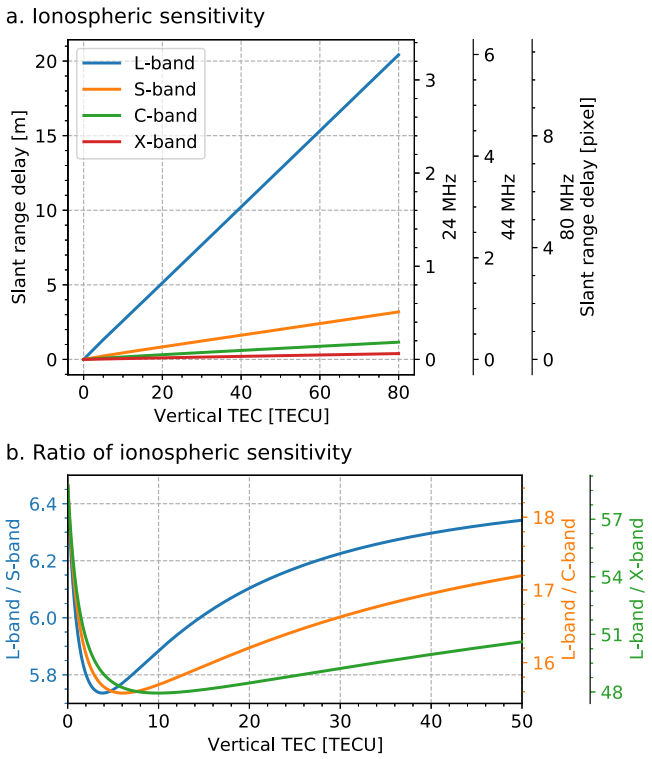

Fig. 7. Ionospheric range delay as a function of vertical TEC. (a) Ionospheric delay for different radar frequencies and different range bandwidths. (b) Ratio of the ionospheric sensitivity between L-band and S-, C-, and X-bands. Calculations are based on equation (6)–(11) assuming a constant incidence angle of 42° of the LOS vector on the ground.

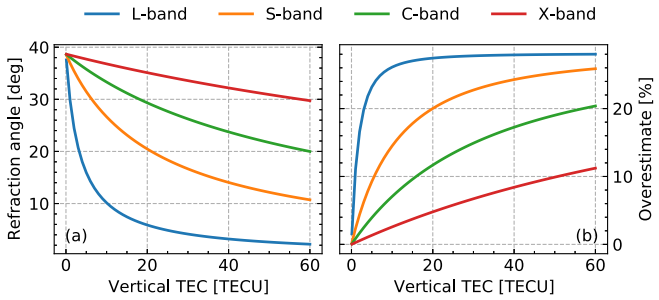

Fig. 8. Impact of refraction on ionospheric range delay as a function of the vertical TEC for a constant incidence angle of 42° on the ground. (a) Refraction angle of the LOS vector at IPP based on equation (8)–(11). (b) Percentage of overestimated ionospheric range delay for ignoring the refraction effect. Lines are color coded for different radar frequencies.

3) Nonlinear Ratio of Ionospheric Sensitivity: Due to the dispersive nature of the ionospheric refraction [equation (9)], the resulting ionospheric range delay is a nonlinear function of the vertical TEC [equation (10)]. The deviation from linearity is small for each radar frequency alone [Fig. 7(a)], but is obvious in the ratio of the ionospheric sensitivity between different frequencies, as shown in Fig. 7(b). The ratios decrease rapidly with increasing VTEC until ∼5 TECU, then slowly increase. For VTEC less than 100 TECU, the ionospheric range delay at the L-band is ∼6 (5.7–6.5)×, ∼17 (15.6–18.4)×, and ∼51 (47.9–58.7)× larger than the S-, C-, and X-bands, respectively.

4) Impact of Refraction on Ionospheric Range Delay: Fig. 8(a) shows the refraction angle of the LOS vector at IPP as a function of the vertical TEC for different radar frequencies given a constant incidence angle of 42° on the ground. A vertical TEC of 20 TECU leads to a refraction angle of 6°, 20°, 29°, and 35° at IPP for the L-, S-, C-, and X-bands, respectively. Ignoring the refraction effect (e.g., in [39]) for the same amount of ionosphere would result in an overestimated ionospheric range delay by 27%, 20%, 12%, and 5% for the L-, S-, C-, and X-bands, respectively [Fig. 8(b)].

TABLE I

SUMMARY OF RESOLUTIONS AND INTERPOLATION METHODS OF THE USED GLOBAL IONOSPHERIC MAPS

GIM	Spatial resolution [lat × lon]	Temporal resolution	Latency [rapid / final solution]	Interpolation [space / time domain]
CLR	2.5° × 5°	1-hour	1 / 11 days	bilinear / linear (rotate)
JLR	2.5° × 5°	2-hour	1 / 11 days	bilinear / linear (rotate)
JHR	1° × 1°	15-min	N/A	bilinear / nearest

C. Global Ionospheric Maps

We use three versions of GNSS-based GIM derived from the VTEC solution of CODE (University of Bern, Bern, Switzerland) and JPL (Jet Propulsion Laboratory, Pasadena, CA, USA) [37], [40]: the CODE low-resolution (CLR) GIM, the JPL low-resolution (JLR) GIM, and the JPL high-resolution (JHR) GIM. The spatial and temporal resolutions of the three GIM products are summarized in Table I. CLR and JLR GIM are publicly available on NASA's Archive of Space and Geodesy Data[3] under the umbrella of the International GNSS Service (IGS) [38]. JLR and JHR GIM use the same GNSS data from ∼200 globally distributed stations and the same cubic C2 basis function [40], but produce snapshot outputs at different spatial and temporal resolutions using associated coefficients.

In order to extract the vertical TEC for the point of interest (e.g., IPP) from the gridded GIM maps, we apply a bilinear interpolation in the space domain. After the spatial interpolation, to estimate the VTEC at the exact SAR acquisition time from CLR and JLR products (with 2-hour temporal resolution), we apply a linear interpolation in the time domain on the rotated TEC maps along the longitude direction to compensate for the strong correlation between the ionosphere and the Sun's position [41]. For JHR GIM (with 15-min temporal resolution), we use nearest neighbor interpolation in time.

D. Topside and Sub-Orbital TEC

The GIM products, derived from the GNSS satellites at an altitude of ∼20 200 km, measure a much thicker ionosphere than the one that radar signal propagates through, which is a thinner portion of ionosphere between the SAR satellite orbit, at an altitude of ∼500–800 km, and ground. Therefore we need to account for the TEC above the SAR satellite orbit up to the GNSS orbit, hereafter called topside TEC. By subtracting the topside TEC from GIM TEC, the sub-orbital TEC, which represents the TEC from SAR sensor to ground, can be obtained.

[3]https://cddis.nasa.gov/archive/gnss/products/ionex/

Topside TEC can be measured from GNSS receivers onboard the low Earth orbiter satellites [42]. We use the dual-frequency data from the global positioning system (GPS) receivers onboard the Sentinel-1A/B with a data rate of 1/10 second to derive the relative LOS TEC between SAR satellites and GPS satellites at the topside piercing point (TPP) of 1800 km. With bias estimations for GPS satellites [37], [40] and receivers [42] as well as the slant-to-vertical conversion, topside TEC can be computed at multiple TPPs depending on different receiver-to-satellite radio links, as shown in Fig. 5. The available topside observations are culled within a range of 10-min centered at the SAR acquisition time and with an elevation cutoff angle of 45° to constrain the possible error during the slant-to-vertical conversion. Then, the sub-orbital TEC at each TPP is obtained by subtracting topside TEC from JHR GIM TEC. Sub-orbital TEC at the TPP that is nearest to the concerned IPP is chosen and used.

Fig. 9 shows the vertical topside, sub-orbital and total TEC along the Sentinel-1A/B orbits on October 19, 2019 (close to solar minimum) and September 28, 2015 (close to the last solar maximum). The estimations show that topside TEC is larger at a sampled date close to the last solar maximum period compared with the one during the solar minimum period. The topside TEC and total TEC show a similar spatial pattern with different magnitudes. The topside TEC varies spatially from 0 to 12 TECU, while the total TEC varies from 0 to 50 TECU.

E. Spatial and Temporal Variations of Ionosphere

The absolute value of ionospheric TEC mainly depends on the status of the solar cycle, which has a period of approximately 11 years, seasons, the time of the day, and the geomagnetic location. The last peak of the solar cycle occurred in April 2014 and the next peak is expected to be around July 2025 +/− eight months [43]. In order to understand the spatial and temporal variation of the magnitude of ionospheric range delay, we analyze the JLR GIM from 2014 to 2019 (solar maximum to solar minimum). Using the expected science orbits of NISAR, we derive a six-year-long time series of daily vertical TEC and the corresponding ionospheric range delay for the L-band SAR for the scene center of each expected NISAR science frame.

Fig. 10 shows the global distribution of the annual median and median absolute deviation (MAD) of VTEC and equivalent range delay at NISAR's L-band in the expected NISAR ascending and descending orbits over 2014 (last solar maximum) and 2019 (solar minimum). NISAR descending orbits (dusk side with ∼6 P.M. local solar time) are expected to experience stronger ionospheric effects than the ascending orbits (dawn side with ∼6 A.M. local solar time). In 2014 (solar maximum), the annual median VTEC varies spatially from 7.3 to 73.6 TECU (1.9–18.8 m of range delay) for descending orbits [Fig. 10(b)] versus 6.7–20.6 TECU (1.8–5.3 m of range delay) for ascending orbits [Fig. 10(a)]. While the spatial pattern of the annual median VTEC remains similar among different years, the overall magnitude decreases from 2014 to 2019 [Fig. 10(e) and (f)] with the spatial variation

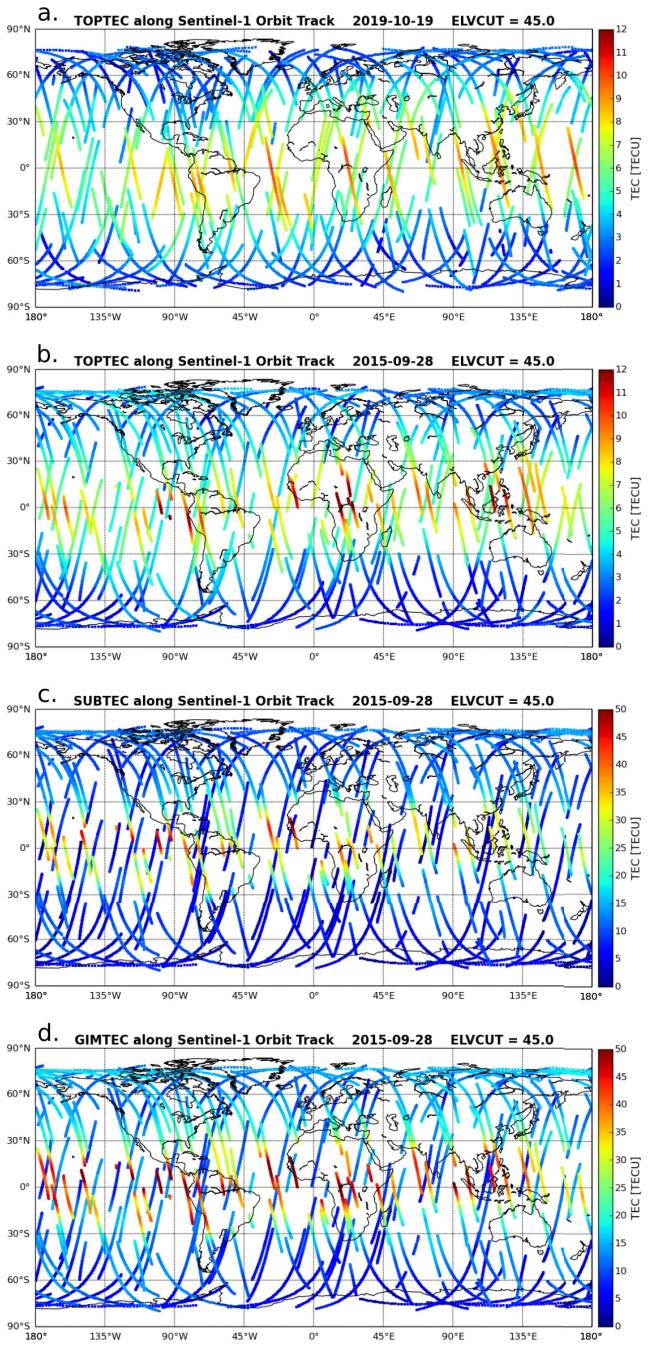

Fig. 9. GNSS-based vertical TEC along Sentinel-1A/B orbits on October 19, 2019 (close to solar minimum) and September 28, 2015 (close to the last solar maximum). (a) and (b) Topside TEC (from SAR orbits to GNSS orbits). (c) Sub-orbital TEC (from the ground to SAR orbits). (d) Total TEC (from the ground to GNSS orbits). ELVCUT: elevation cutoff angle in degrees. The 10-min window culling is not applied. The data discontinuity at some locations and/or times may be caused by the elevation angle cutoff, inadequate amount of data for averaging or fitting, and possible removal of noisy data.

of 2.7–22.4 TECU (0.8–5.7 m of range delay) for descending orbits [Fig. 10(d)] and of 1.9–10.0 TECU (0.5–2.6 m of range delay) for ascending orbits [Fig. 10(c)]. There is an overall good spatial correlation between the annual magnitude (annual median) and the seasonal variation (annual MAD), as shown in Fig. 10 bottom panel.

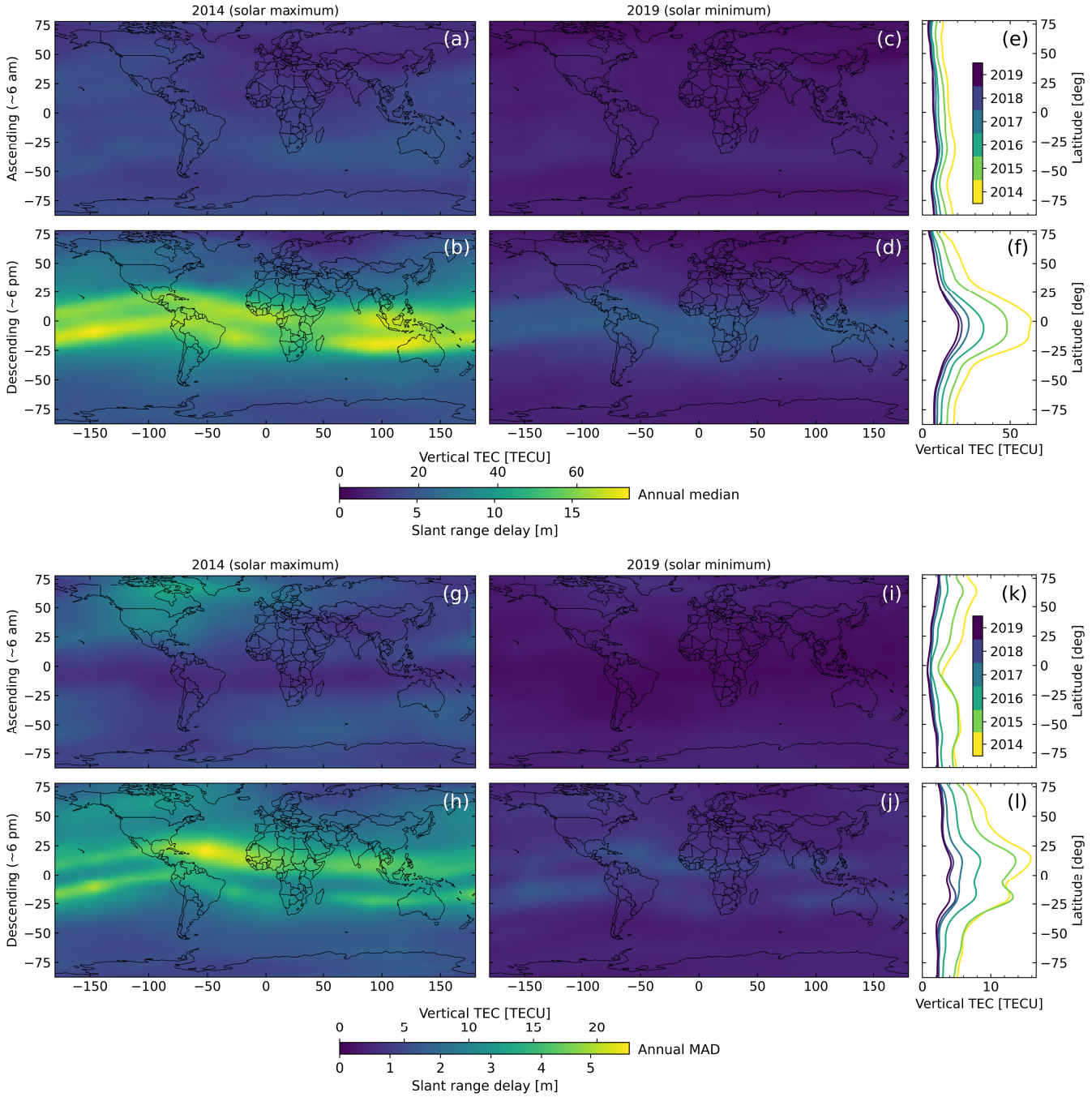

Fig. 10. Global distribution of ionospheric range delays during the last half solar cycle (from 2014 to 2019) based on the expected science orbits of NISAR (6 A.M. ascending and 6 P.M. descending nodal times) using JLR GIM. Top and bottom panels: the annual median and MAD of vertical TEC, respectively. Profiles on the right: the average vertical TEC variation along the latitude for each year. The corresponding slant range delay (range geolocation error) is calculated based on the NISAR L-band frequency with an incidence angle of 42° of the LOS vector on the ground. For the NISAR S-band SAR, the range delay will be ~6× smaller in magnitude. For Sentinel-1 with the similar dusk/dawn acquisition strategy, the ionospheric impact will be similar but with relatively stronger effects on its ascending orbits and with ~17× smaller magnitude in range delay.

The range delay in Fig. 10 can be scaled roughly by ~1/6 for the NISAR S-band and by ~1/17 for the C-band data, or precisely using equation (6)–(11) to account for the nonlinear ratio of ionospheric sensitivity (Section IV-B3). Note that for Sentinel-1, after scaling to the C-band, one needs to swap ascending and descending labels in Fig. 10 to represent the dawn/dusk acquisition strategy of Sentinel-1 which is opposite to dusk/dawn acquisition strategy of NISAR.

V. Mis-Registration From SAR Offset Time Series for the Relative Geolocation Accuracy Evaluation

We estimate the mis-registration time series from a stack of SLCs coregistered using pure geometry (precise orbits and DEM) for the evaluation of the relative geolocation accuracy. SAR can measure the relative shift between image pairs using speckle tracking [8]. This approach is usually based on the

cross-correlation of speckle patterns from complex or intensity images [44]. The relative shift is referred to as offsets. Given a stack of offset pairs, an offset time series can be estimated using the small baseline analysis technique, adapted from InSAR [45], to mitigate the impact of decorrelation [46]. A fully connected network should be used to ensure an unbiased estimation. A median filter is usually applied to the estimated offset field to smooth out the high spatial frequency noise [47].

There are a few practical considerations for the time series estimation of SAR offset, different from the one for the InSAR phase [48]. First, offsets are spatially absolute measurements, thus, do not require spatial referencing before the time series estimation. Second, in the computational aspect, zero values are common and valid offset estimates due to the limited quantization precision of speckle tracking, which can be described as

$$\sigma_{\text{xcorr}}^{\text{qnt}} = \frac{\Delta}{\Omega_{\text{SLC}} \cdot \Omega_{\text{corr}}} \tag{13}$$

where Δ represents the pixel spacing in the range or azimuth direction, and Ω_{SLC} and Ω_{corr} represent the oversampling factors applied to the SLC image before cross-correlation and to the correlation surface, respectively. Given typical values of $\Omega_{\text{SLC}} = 2$ and $\Omega_{\text{corr}} = 64$, $\sigma_{\text{xcorr}}^{\text{qnt}}$ is 1.8 and 11.0 cm for Sentinel-1 in range and azimuth directions, respectively. Thus, any offsets with a magnitude smaller than $\sigma_{\text{xcorr}}^{\text{qnt}}/2$ (0.9 cm in range direction and 5.5 cm in azimuth direction) will be rounded to zero, which could be common in practice. While for the InSAR phase, the rounding-to-zero scenario is extremely unlikely due to its significantly higher quantization precision. Third, we evaluate the post-inversion quality of the estimated offset time series using the L_2-norm residual normalized by the pixel spacing and discard pixels with residual values larger than a predefined threshold, e.g., 0.25.

VI. Experimental Results

We evaluate the relative geolocation accuracy of the MAGIC approach (with the offset from model prediction as outlined in Sections III and IV), using the offset from the cross-correlation approach (Section V) as the reference (observation). Test data includes two stacks of the C-band Sentinel-1 TOPS data (ascending track 149 with 104 acquisitions and descending track 156 with 201 acquisitions) from 2014 to 2020 in northern Chile and a stack of the L-band ALOS-2 stripmap ultrafine mode data (descending track 23 with 49 acquisitions) from 2015 to 2019 in Kyushu, Japan [49]. The topside TEC estimated from Sentinel-1A/B is not accounted for here but is used and discussed in detail in Section VII-C.

We use the topsStack [11] and stripmapStack [12] processors to coregister the stacks of Sentinel-1 and ALOS-2 SLCs with pure geometry (precise orbits and DEM), respectively, and use the GPU-based PyCuAmpcor[4] to compute small baseline offset pairs; all are within the ISCE software [18]. For Sentinel-1, we use the SRTM DEM (SRTMGL1, 1 arc second with void-filled, ~30 m) [50]; pair each SAR image with its three nearest neighbors in time (sequential network); estimate each offset map using an estimation window size of 256×128 pixels and a skip size of 300×100 pixels between windows in the range and azimuth directions, respectively. For ALOS-2, we use the DEM released by the Geospatial Information Authority of Japan, Tsukuba, Japan (GSI, 0.4 arc second, ~10 m); select offset pairs with small temporal (400 days) and spatial baselines (200 m); estimate each offset using an estimation window size of 256×256 pixels and a skip size of 100×80 pixels between windows in the range and azimuth directions, respectively. For all the offset estimations, we oversample the SLC images by a factor of 2 before cross-correlation and oversample the correlation surface by a factor of 64 to locate the peak of the correlation surface.

The offset time series is estimated using the small baseline approach as outlined in Section V and implemented in the MintPy software [48]. Pixels with time series estimation residual larger than a predefined threshold (0.125 pixel for Sentinel-1 and 1.0 pixel for ALOS-2) are discarded (12%, 18%, and 16% of pixels for Sentinel-1 ascending track 149, descending track 156, and ALOS-2 descending track 23, respectively). The azimuth offset is estimated but not used.

A. Relative Geolocation Accuracy of C-Band Sentinel-1

Fig. 11 compares the estimated range delay time series from SAR images (observation) with the predicted range delay time series (model prediction) of each geolocation error source progressively for the C-band Sentinel-1 ascending track 149 in Chile. Fig. 11 top panel compares the estimated range delay from SAR (blue solid line) with the predicted range delay from ionosphere using TEC products from JHR GIM (dashed orange line), JLR GIM (dotted gray line), and CLR GIM (dash-dotted black line). The impact of the ionosphere is strong for the Sentinel-1 ascending orbit at low geomagnetic latitude areas [51]. In this case, it is clear and obvious that the ionosphere dominates the observed range delay in SAR data with a very high coefficient of determination R^2 of 0.91 [Fig. 11(b)]. The large magnitude of range delays (up to 0.7 m) during 2015 is due to the strong solar activities around the last solar maximum in 2014. The maximum peak to valley range delay is 1.0 m, about half the range pixel size of Sentinel-1 in IW mode (2.3 m). After correcting for ionosphere using JPL high-resolution GIM, the RMSE of the SAR range delay time series decreased from 20.2 to 8.7 cm. The observed range delay from SAR matches significantly better with the predicted range delay from JPL high-resolution GIM (RMSE of 8.7 cm) than the low-resolution GIM from JPL and CODE (with RMSE of 20.7 and 22.8 cm).

Fig. 11 central panel demonstrates that after correcting for ionospheric delay using JHR GIM, the residual range delay is dominated by the SET with a high R^2 of 0.64. The SET time series has a periodic temporal variation with a cycle of 64.1 days [5.7 cycles per year; Fig. 11(c)] due to the frequency aliasing as explained in Section III-E1. Fig. 11 bottom panel compares the SAR observation after correcting for ionosphere and SET with the predicted tropospheric delay using the ERA5 global atmospheric model. The RMSE of the range delay time series decreased from 8.7 to 7.1 cm after correcting for SET, then increased slightly to 7.8 cm after correcting for the troposphere.

[4]https://github.com/isce-framework/isce2/tree/main/contrib/PyCuAmpcor

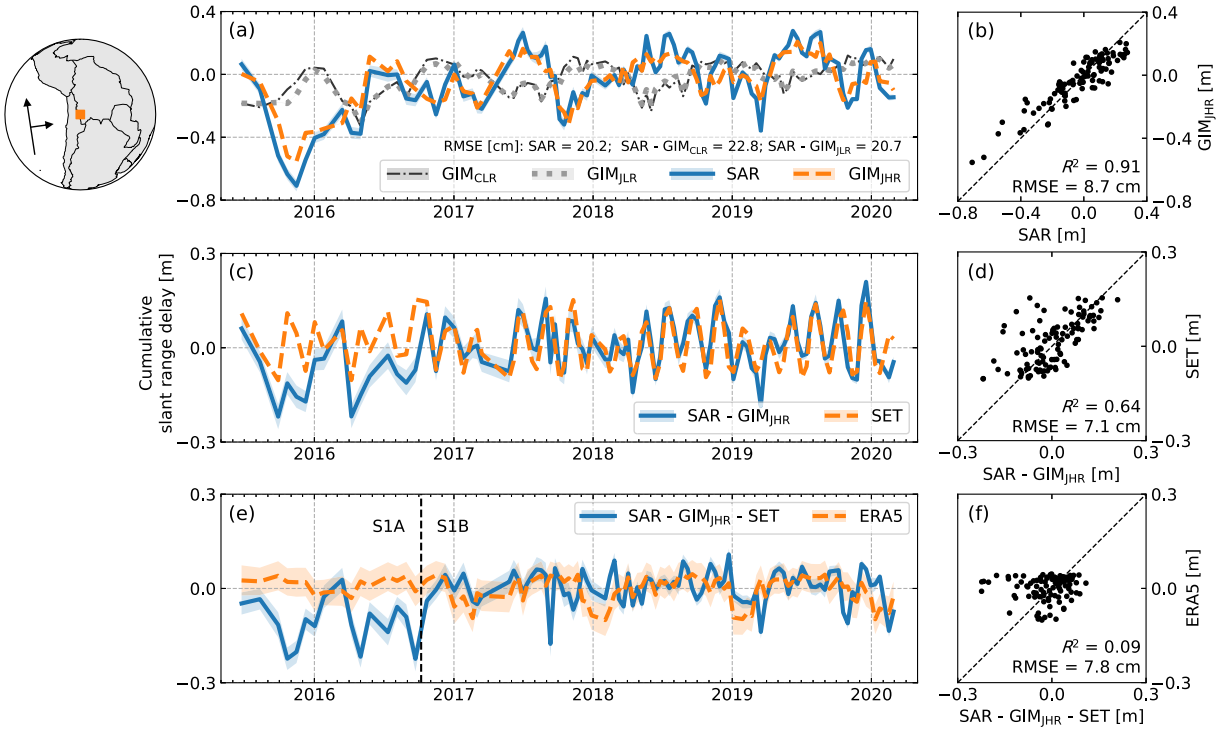

Fig. 11. Progressive comparisons between the observed and predicted relative range geolocation errors for the C-band Sentinel-1 ascending track 149 in Chile. Upper left inset: dataset location. Top panel: the observed range delay (observation) from SAR image cross-correlation (blue solid line) versus the predicted range delay from the ionosphere (model prediction) using JHR GIM (dashed orange line), JLR GIM (dotted gray line), and CLR GIM (dash-dotted black line). Central panel: the observation after correcting for ionosphere using JHR GIM versus the model prediction from SET. Bottom panel: the observation after correcting for ionosphere and SET versus the model prediction from troposphere using ERA5. For each panel, the observation time series is shifted by its median value, the model prediction time series is shifted by its median difference with the observation. The median value and the three times MAD range within a window of 20 × 20 pixels centered at [S21.30°, W67.39°] are used. SAR acquisition at 23:07 UTC (∼6 P.M. local solar time).

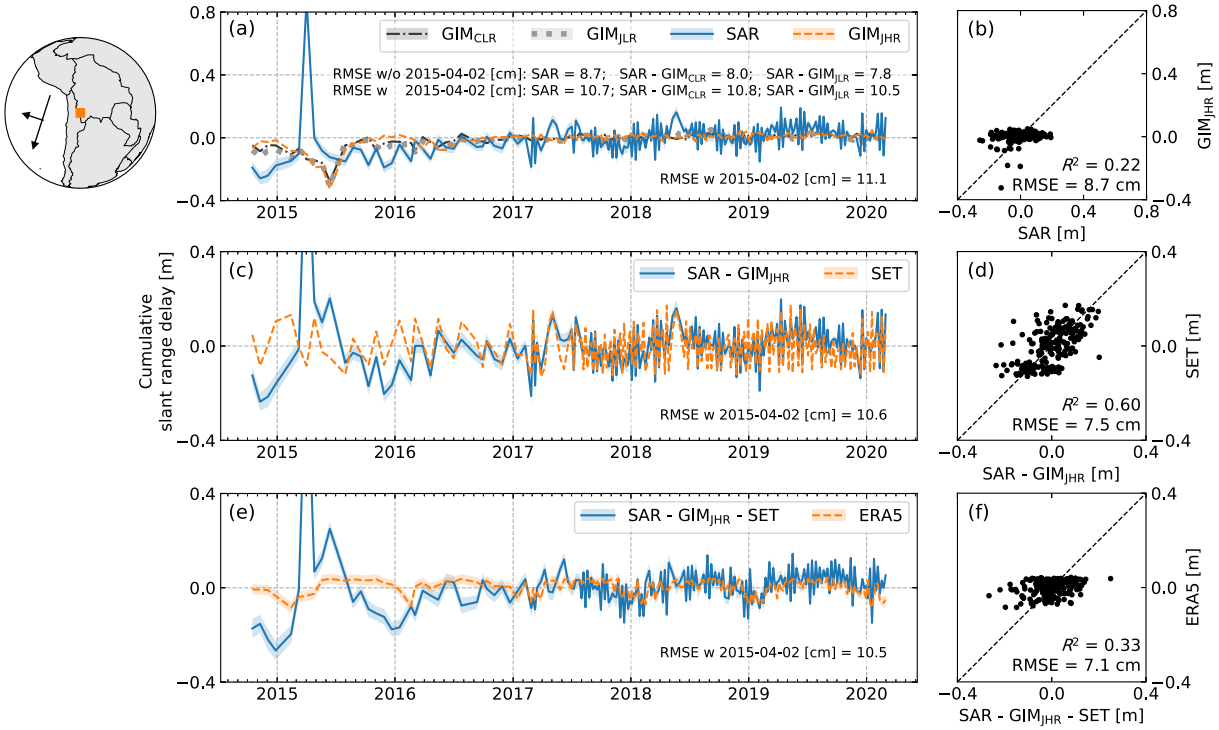

Fig. 12. Similar to Fig. 11, but for the C-band Sentinel-1 descending track 156 in Chile with SAR acquisition at 10:00 UTC (∼6 A.M. local solar time).

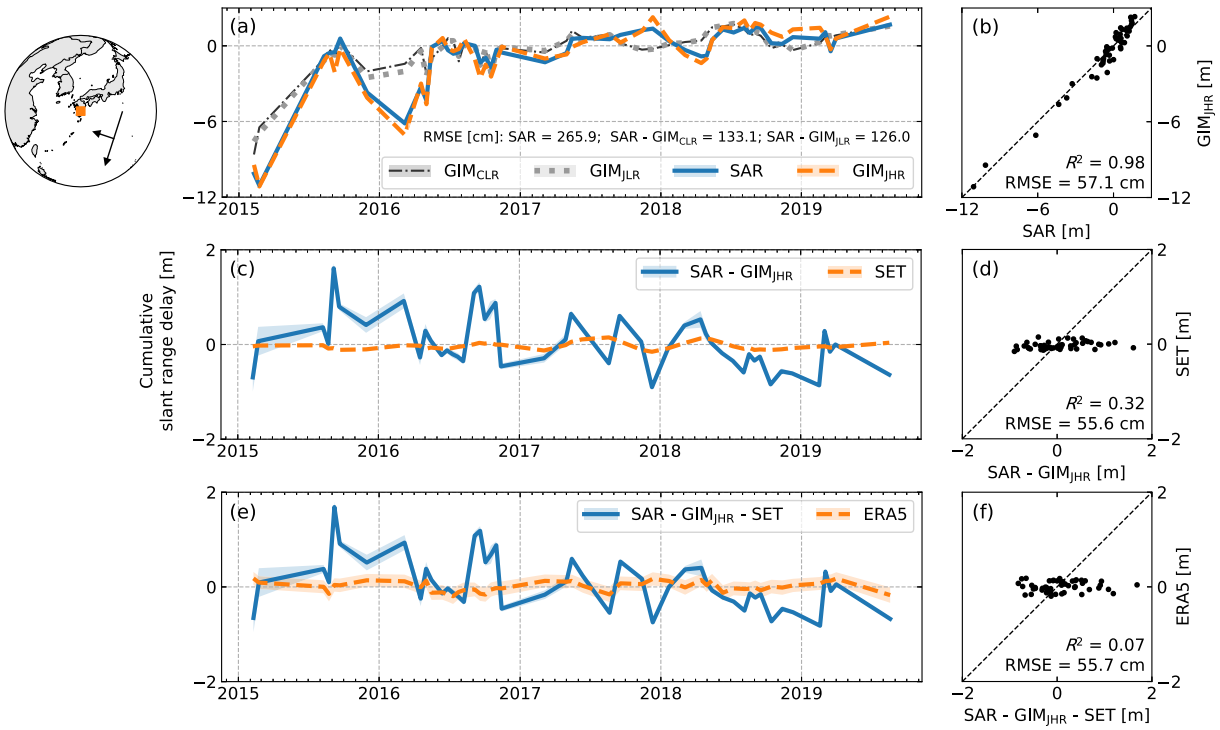

Fig. 13. Similar to Fig. 11, but for the L-band ALOS-2 descending track 23 in Japan with SAR acquisition at 03:19 UTC (∼12 P.M. noon local solar time). The median and MAD values from the whole image are used.

The range delay time series for the descending track 156 (Fig. 12) shows much smaller variation than the ascending track (10.7 cm versus 20.2 cm) due to the weaker ionosphere at 6 A.M. All three GIM give similar range delay predictions with RMSE after correction of 10.8, 10.5, and 11.1 cm for CLR, JLR, and JHR GIM, respectively [Fig. 12(a)]. The similar performance is likely due to: 1) the SAR acquisition time is at 10:00 UTC when all GIM have products, thus, little impact from different temporal resolutions on the GIM estimation and 2) the ionosphere has a much smaller daily variation at 6 A.M. local solar time. Without strong ionospheric impact, SET becomes the dominant source of relative geolocation errors [Fig. 12(c)]. Since the middle of 2017, the regular interleaving of Sentinel-1A and Sentinel-1B reduced the sampling interval from 12 days to 6 days, resulting in an aliased SET frequency of 14.8 days (24.7 cycles per year), as observed in Fig. 12(c). Note that there is an abnormally high range delay of 0.8 m on April 2, 2015, which cannot be explained by ionosphere or Earth motions; therefore, we speculate it originated from the SAR data processing. After excluding the outlier on April 2, 2015, the RMSE of the range delay time series changed from 8.7 to 8.7, 7.5, and 7.1 cm after correcting for ionosphere, SET, and troposphere, respectively. The final RMSE of the descending track time series (7.1 cm) is similar to the one from the ascending track (7.8 cm).

B. Relative Geolocation Accuracy of L-Band ALOS-2

The L-band ALOS-2 time series in Japan (Fig. 13) shows a maximum range delay of 11.1 m. The temporal variation is dominated by the ionosphere with large delays during 2015 and 2016 due to strong solar activities [Fig. 13(a)] and with a very high coefficient of determination of 0.98 [Fig. 13(b)], similar to the Sentinel-1 ascending track 149 [Fig. 11(a)]. Both CLR and JLR GIM predictions match well with the SAR observation; however, JHR GIM prediction matches significantly better with a reduction of the time series RMSE from 265.9 to 57.1 cm. After correcting for SET and troposphere, the time series RMSE further decreased slightly to 55.6 and 55.7 cm, respectively, indicating marginal improvements.

The final residual range delay time series after all the corrections (ionosphere, troposphere, and SET), i.e., the difference between solid blue lines and dashed orange lines in Fig. 13(e), is in the meter scale with the maximum peak to valley delay of 2.6 m, much larger than the temporal variation of possible contributions from tropospheric turbulence or other Earth motions (OTL, pole tides, and so on) that we have not accounted for. Thus, we interpret this large residual range delay as the possible remaining contributions from the ionosphere, especially topside TEC from ALOS-2 SAR satellite orbit at ∼630 km to GNSS satellite orbit at ∼20 200 km and discuss in more detail in Section VII-C and VII-G.

VII. DISCUSSION

A. Range Bias Between Sentinel-1A and Sentinel-1B

We observed a temporally consistent bias between S1A and S1B in the residual range delay after correcting for SET and troposphere, as shown in Fig. 14(a) for the descending track 156. With acquisitions from both platforms regularly interleaving with each other, we apply a linear fit to the time series for each platform and solve for the difference in the intercepts as

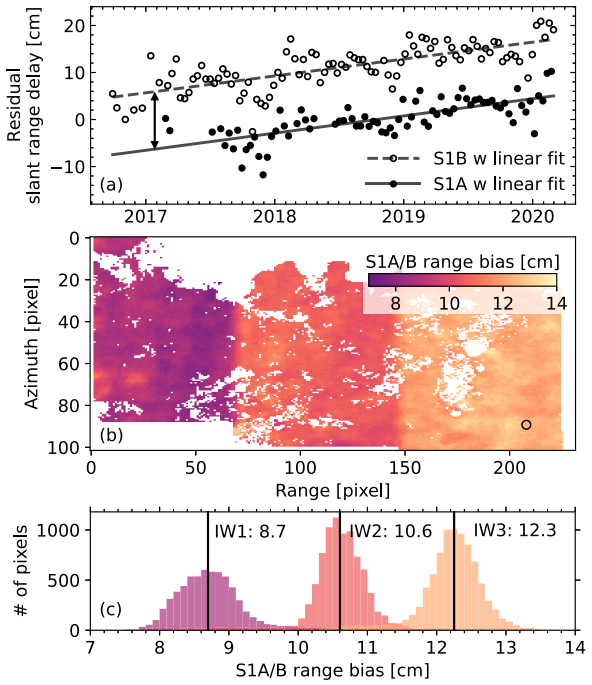

Fig. 14. Range bias between S1A and S1B. (a) Residual range delay time series after correcting for SET and troposphere for one pixel [black circle in (b)] in Sentinel-1 descending track 156 in Chile. Only the time period with both platforms regularly acquiring images (from September 29, 2016 to February 29, 2020; 77 and 97 images from S1A and S1B, respectively) is shown and used for the bias estimation. (b) Map of the estimated range bias. (c) Histogram of (b) for each subswath with black vertical line for the median value.

the bias estimate. The bias has a subswath dependence with median values of 8.7, 10.6, and 12.3 cm for IW1, IW2, and IW3, respectively [Fig. 14(b) and (c)]. Similar bias observations of ∼15 cm have been reported by Gisinger *et al.* [16] and Solgaard *et al.* [52] after the Extended Timing Annotation Dataset (ETAD) correction. Since the ETAD correction is designed to correct the effects of focusing approximations, the presence of the bias after the ETAD correction in [16] implies that the bias may not be due to the focusing approximations applied during the Sentinel-1 SAR processing.

After correcting for the S1A/B range bias using the empirically estimated values above, the final RMSE of the range delay time series after correcting for ionosphere, SET, and troposphere reduced from 7.8 to 6.4 cm for the ascending track 149 and from 7.1 to 5.7 cm for the descending track 156. More investigations are needed to confirm whether the empirically estimated values of the S1A/B bias are applicable to other regions and whether the subswath dependence exists after the ETAD correction. Discussions hereafter assume the S1A/B range bias has been removed.

B. Summary of Geolocation Error Corrections

The relative geolocation accuracy of the three SAR datasets after bias corrections is summarized in Fig. 15 and Table II. In general, the accuracy improves after correcting for each of the geolocation errors from the ionosphere, SET, and troposphere, as shown in the decreasing RMSE values and

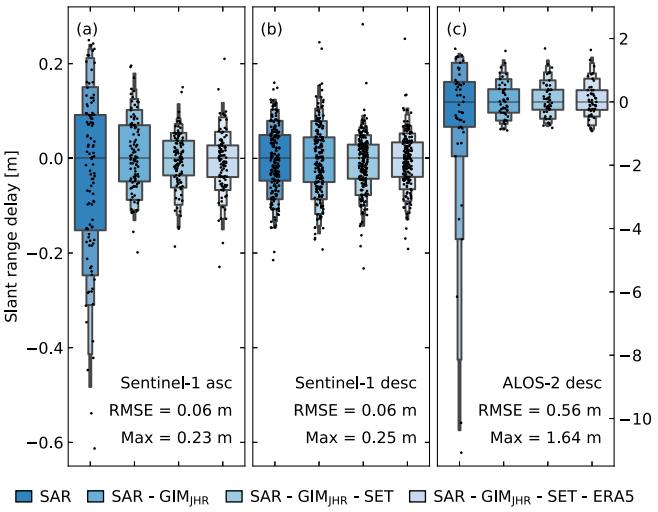

Fig. 15. Distribution of the relative range delay time series after routine geolocation error corrections. The letter-value plot [53] shows up to 95% of the data overlaid by the scatter plot showing all the data. Labels describe the relative geolocation accuracy in range direction in terms of RMSE and maximum magnitude. For Sentinel-1 in (a) and (b), the S1A/B range bias has been removed. For Sentinel-1 descending track in (b), the outlier acquisition on April 02, 2015, is excluded.

TABLE II

RELATIVE GEOLOCATION ACCURACY IN RANGE DIRECTION IN TERMS OF RMSE AND MAXIMUM MAGNITUDE FOR SENTINEL-1 AND ALOS-2 AFTER ROUTINE CORRECTION FOR EACH OF THE GEOLOCATION ERRORS

RMSE [cm] (Maximum)	SAR	SAR - GIM$_{JHR}$	SAR - GIM$_{JHR}$ - SET	SAR - GIM$_{JHR}$ - SET - ERA5
Sentinel-1 asc.	18.3 (61)	8.0 (20)	5.8 (19)	6.4 (23)
Sentinel-1 desc.	7.1 (21)	7.4 (25)	6.1 (28)	5.7 (25)
ALOS-2 desc.	265.9 (1108)	57.1 (161)	55.6 (169)	55.7 (164)

[1] For Sentinel-1, the S1A/B range bias has been removed.
[2] For Sentinel-1 descending, outlier acquisition at 2015-04-02 is excluded.

decreasing interquartile ranges in Fig. 15, for all three datasets. The three exceptions, ERA5 tropospheric corrections for ALOS-2 descending track and Sentinel-1 ascending track, and JHR GIM ionospheric correction for Sentinel-1 descending track, have negligible RMSE increases of 1, 6, and 3 mm, respectively.

The ionosphere is the dominant contributor of geolocation errors for the L-band ALOS-2 ($R^2 = 0.98$) and the C-band Sentinel-1 ascending (dusk side) orbit ($R^2 = 0.91$), while SET is the second largest. For the C-band Sentinel-1 descending (dawn side) orbit where the ionosphere is weak, SET become the largest.

Following a routine correction procedure of S1A/B bias (for Sentinel-1), JHR GIM for ionosphere, SET, and ERA5 for the troposphere, the relative geolocation accuracy of the Sentinel-1 stacks coregistered using geometry is ∼6 cm in RMSE with the maximum residual of 25 cm (outlier acquisition at April 02, 2015, is excluded). We expect even better

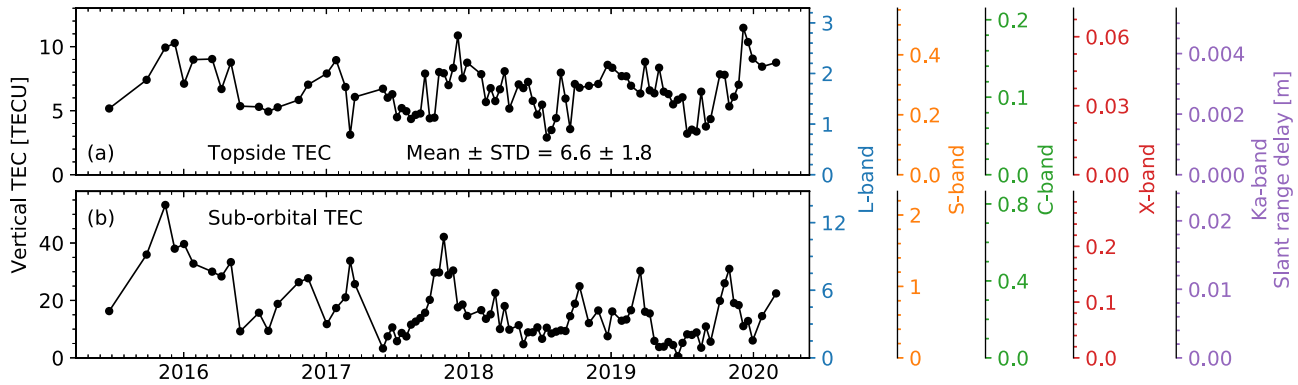

Fig. 16. Impact of topside TEC on the geolocation of the L- (1.257 GHz, NISAR), S- (3.2 GHz, NISAR), C- (5.405 GHz, Sentinel-1), X- (9.65 GHz, TerraSAR-X), and Ka-bands (35.75 GHz, SWOT) SAR at ~6 P.M. local solar time. (a) Estimated topside TEC time series using GPS receivers onboard Sentinel-1 platforms for the ascending track 149 at ~6 P.M. local solar time. (b) Estimated sub-orbital TEC as the difference between the total TEC from JHR GIM and topside TEC. Axes on the right: predicted range delay for different radar carrier frequencies assuming an incidence angle of 42° of the LOS vector on the ground following equation (6)–(11).

accuracy after incorporating ETAD for Sentinel-1 SAR processing effects [16]. For ALOS-2, the relative geolocation accuracy is 0.56 m with a maximum value of 1.64 m.

C. Impact of Topside TEC on SAR Geolocation

We evaluate the impact of the topside TEC on SAR geolocation using the GPS receivers onboard Sentinel-1 platforms, as described in Section IV-D. Fig. 16 shows the topside and sub-orbital TEC for Sentinel-1 ascending track 149 in Chile at ~6 P.M. local solar time. Topside TEC has a much smaller temporal variation (3–11 TECU) than the sub-orbital TEC (2–51 TECU). The nonzero lower boundary of the topside TEC time series indicates that there is always an absolute geolocation bias due to topside TEC if not accounted for while using the GNSS-based TEC products.

Fig. 16 right-hand side shows the expected topside ionospheric range delay for different radar frequencies at the L- (NISAR), S- (NISAR), C- (Sentinel-1), X- (TerraSAR-X), and Ka-bands (SWOT) assuming an incidence angle of 42°. The 6.6±1.8 TECU of topside TEC could lead to a geolocation error of 1.7 ± 0.46 m for the L-band, 30.6 ± 7.8 cm for the S-band, 11.5 ± 3.0 cm for the C-band, 3.8 ± 1.0 cm for the X-band, and 2.8 ± 0.8 mm for the Ka-band. For coregistration, the 1.8 TECU of topside TEC variation in standard deviation would result in 0.07, 0.14, and 0.25 pixel of range misregistration for the L-band SAR with range bandwidths of 24, 44, and 80 MHz, respectively; and result in 0.04, 0.013, 0.007, and 0.001 pixels for the S-, C-, X-, and Ka-bands with range bandwidths of 75 (NISAR), 64.35 (Sentinel-1), 109.89 (TerraSAR-X), and 200 MHz (SWOT), respectively.

After correcting for topside TEC, the final RMSE of the C-band Sentinel-1 ascending track 149 reduced from 6.4 to 4.9 cm (Appendix). Assuming the same noise level of topside TEC (with range delay STD of 46.2 cm for the L-band), the expected final RMSE using sub-orbital TEC for the L-band SAR can be derived as $((55.7)^2 - (46.2)^2)^{1/2} = 31.1$ cm.

D. Comparing Different GNSS-Based TEC Products

We evaluate the performance of different GNSS-based TEC products based on the relative geolocation accuracy in range direction. The result is summarized in Table III. The JPL high-resolution GIM shows significantly better performance than the low-resolution GIM from JPL or CODE for Sentinel-1 ascending (dusk side) orbit and the L-band ALOS-2 when the ionosphere is strong. The higher spatial and temporal resolution of the JHR GIM appears to better capture the highly structured ionospheric regions, such as the equatorial ionization anomaly (EIA) crests and trough, and their temporal variations than the low-resolution ones. The performance even further improves when we account for topside TEC. The performance of JHR GIM is similar to the low-resolution GIM for the Sentinel-1 descending (dawn side) orbit when ionospheric TEC is low and its variation is small. This is likely due to the SAR acquisition time at 10:00 UTC in this example coinciding with the sampling time of the low- and high-resolution GIM models; therefore, the impact of the higher temporal sampling (15-min versus 2-hour) cannot be justified.

TABLE III
COMPARISON BETWEEN DIFFERENT GNSS-BASED TEC PRODUCTS ON THE RELATIVE GEOLOCATION ACCURACY IN RANGE DIRECTION IN RMSE AFTER SET AND TROPOSPHERIC CORRECTION

RMSE [cm]	No TEC	GIM_{CLR}	GIM_{JLR}	GIM_{JHR}	TEC_{sub}
Sentinel-1 asc.	18.1	21.2	19.2	6.4	4.9
Sentinel-1 desc.	5.7	5.1	5.1	5.6	N/A
ALOS-2 desc.	271.2	138.1	131.3	55.7	31.1*

[1] For Sentinel-1, the S1A/B range bias has been removed.
[2] For Sentinel-1 descending, outlier acquisition at 2015-04-02 is excluded.
* Expected value after correcting for topside TEC based on section VII-C.

E. Adaptive Scaling of Total TEC for Sub-Orbital TEC

The ratio of topside TEC to total TEC for the site in northern Chile (Fig. 17) shows a wide range of temporal variation (0.14–0.78) with a median value of 0.31. There is a clear seasonal variation with peaks during May–August and December. Note that the slightly increasing overall ratio from the solar maximum year (2015) to the solar minimum year (2019) is due to the relatively weaker activities in the sub-orbital ionosphere [Fig. 16(b)]. This observation implies

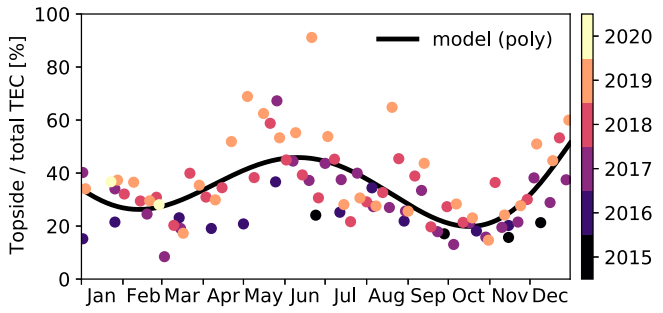

Fig. 17. Ratio of topside TEC to total TEC for the C-band Sentinel-1 ascending track 149 in Chile (~6 P.M. local solar time). Median value: 31%. Solid line: polynomial fit as a function of the day of the year.

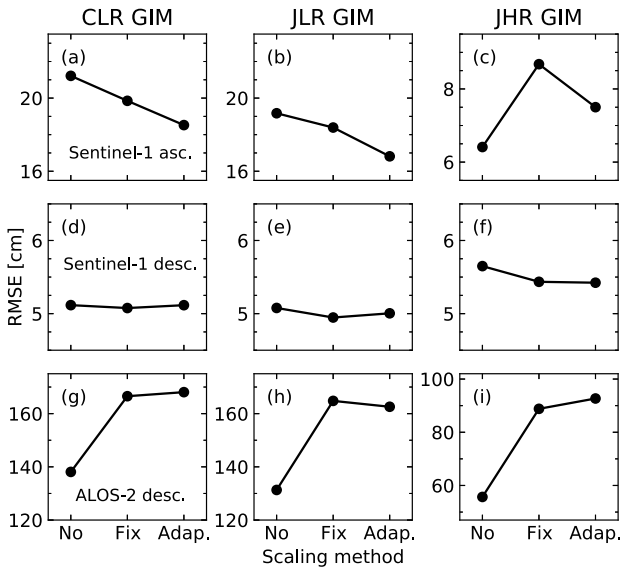

Fig. 18. Comparison among different methods of scaling total TEC to sub-orbital TEC. From top to bottom: Sentinel-1 ascending track 149 in Chile, Sentinel-1 descending track 156 in Chile, and ALOS-2 descending track 23 in Japan, respectively. No: no scaling. Fix: scaling with a fixed ratio. Adap: scaling with an adaptive ratio based on equation (14).

that a data-driven model for the ratio of topside TEC may better represent the topside TEC compared with a constant value that has been used in previous studies, such as in [16].

We test an adaptive scaling approach based on topside TEC estimates from Sentinel-1 ascending track 149 to all three SAR datasets. The seasonal behavior of the topside TEC to total TEC ratio α can be modeled as a function of the day of the year t_d using a sixth-order polynomial as

$$\begin{aligned}\alpha = {} & 34.302124 - 0.342926 \cdot t_d + 2.435454 \times 10^{-3} \cdot t_d^2 \\ & + 4.556585 \times 10^{-5} \cdot t_d^3 - 4.718176 \times 10^{-7} \cdot t_d^4 \\ & + 1.430266 \times 10^{-9} \cdot t_d^5 - 1.391471 \times 10^{-12} \cdot t_d^6. \quad (14)\end{aligned}$$

Fig. 18 compares the relative geolocation accuracy among three different scaling methods: 1) no scaling; 2) scaling with a fixed ratio of 0.69; and 3) scaling with an adaptive ratio based on equation (14). SET, tropospheric delays, and/or S1A/B bias have been corrected for all cases. For Sentinel-1, scaling generally outperforms no scaling, except for JHR GIM

TABLE IV

EXPECTED UPPER BOUND OF THE RANGE GEOLOCATION ERROR BUDGET FOR NISAR AFTER ROUTINE CORRECTIONS FOR IONOSPHERE (GIM), TROPOSPHERE (ERA5), AND SET

Sources	Absolute ± relative accuracy [m] [L-band / S-band]
Ionosphere (total TEC[1])	0.223 ± 1.206 / 0.037 ± 0.215
Ionosphere (topside TEC[2])	1.739 ± 0.517 / 0.307 ± 0.091
Troposphere[3]	0.040 ± 0.050
Tidal Effects[4]	0.000 ± 0.044
Orbital Error[5]	0.005 ± 0.030
DEM Error[6]	4.442 ± 0.002
Overall	6.449 ± 1.314 / 4.832 ± 0.244

[1] Based on JPL low resolution GIM accuracy [38].
[2] Uncompensated topside ionosphere based on this study.
[3] Based on ERA5 and ERA-Int accuracy [56], [57].
[4] Uncompensated tidal effects including ocean tidal loading [32], pole tides [30] and atmospheric loading [33].
[5] Based on Sentinel-1A orbital accuracy [13].
[6] Based on Copernicus DEM accuracy [58].

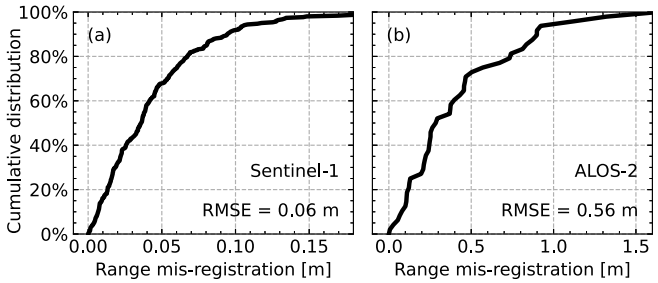

Fig. 19. Cumulative distribution of range mis-registration for geometrical coregistration with model-driven refinement from ionosphere (JHR GIM), troposphere (ERA5), and SET. (a) Sentinel-1 with 304 acquisitions from ascending and descending orbits, excluding the outlier acquisition at April 02, 2015. (b) ALOS-2 with 49 acquisitions from descending orbit.

along the ascending orbit [Fig. 18(c)]; the adaptive scaling outperforms the fixed scaling. For ALOS-2, scaling performs poorer than no scaling, which is expected because both the fixed and adaptive scaling ratios are calculated for Sentinel-1 at ~700 km, which is different from ALOS-2's altitude of ~630 km. Beside seasonality, we expect the ratio of topside TEC depends at least on the latitude and altitude of interest. Thus, such a data-driven model can be useful if more latitude-based topside TEC is estimated for each SAR satellite altitude.

F. Implications for Geometrical Stack Coregistration With Model-Driven Refinement

Fig. 19(a) shows the distribution of Sentinel-1's range mis-registration, i.e., the residual range delay after correcting for S1A/B range bias, ionospheric delay, tropospheric delay, and SET. The range mis-registration RMSE is 0.06 m (0.027 pixels) with 80% of acquisitions experiencing mis-registration of 0.07 m or less. The observed mis-registration is well below 1/10th of the Sentinel-1's IW range pixel spacing, indicating that geometrical offsets refined by model-driven

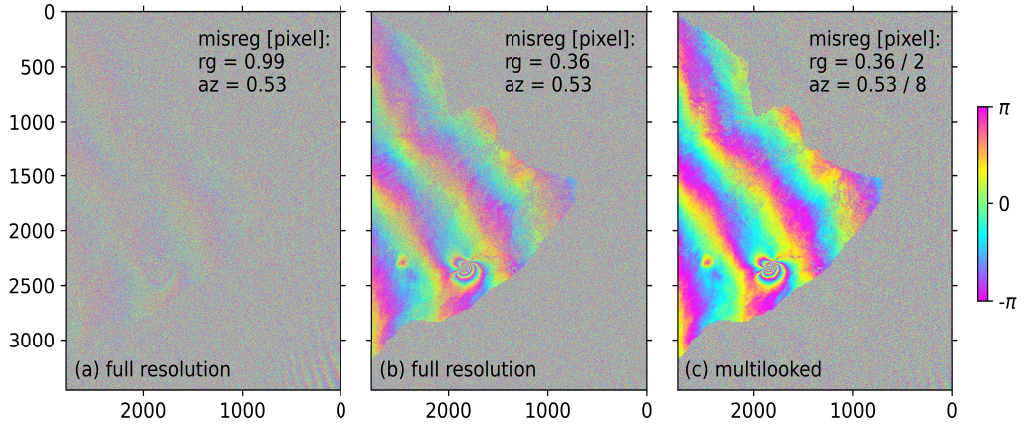

Fig. 20. Interferogram formed from two ALOS SLCs over Hawaii coregistered using geometry (a) without and (b)–(c) with model-driven refinement. (a) and (b) Full resolution interferometric phase. (c) Multilooked interferometric phase (2 and 8 looks in range and azimuth direction, respectively). SAR images are acquired on January 19, 2011 and March 06, 2011 in FBD stripmap mode in descending track 598 frame 3230. Predicted refinement from ionosphere (JHR GIM), troposphere (ERA5), and SET in range direction: 5.87 m.

mis-registrations can align Sentinel-1 stacks with required accuracy in range direction for most applications including interferometry.

Fig. 19(b) shows the distribution of range mis-registration for the L-band ALOS-2 stack with an RMSE of 0.56 m and with 80% acquisitions experiencing mis-registrations up to 0.75 m. The observed RMSE of 0.56 m is equivalent to 0.06 pixel for the ALOS stripmap fine beam double (FBD) polarization mode, 0.38 pixel for ALOS-2 stripmap ultra-fine mode, and 0.09 pixel for the NISAR L-band SAR with 24 MHz of range sampling frequency. Note that with topside TEC correction, the RMSE is expected to be further reduced to 0.31 m, bringing down the range mis-registration to 0.05 pixel for NISAR. Therefore, in the range direction, a pure geometrical coregistration with model-driven refinement, including topside TEC correction, could potentially be sufficient to produce the coregistered stack of SLCs. However, in the azimuth direction, more precise knowledge of the ionosphere, especially the TEC gradient, is needed to evaluate the azimuth geolocation accuracy for the L-band SAR, which is beyond the scope of this study.

Fig. 20 demonstrates the impact of model-driven refinement on geometrical coregistration using two ALOS SLCs in FBD mode over Hawaii. The unfiltered, full-resolution interferogram is noisy and totally decorrelated when SLCs are coregistered using only geometrical offsets (from precise orbits and DEM) with mis-registration errors of 0.99 and 0.53 pixel in the range and azimuth directions, respectively. After applying the model-driven refinement of 5.87 m of range delay predicted from the ionosphere (JHR GIM), the troposphere (ERA5), and SET, the range mis-registration is reduced to 0.36 pixel and the generated interferogram becomes significantly more coherent. The remaining decorrelation is mainly due to the uncorrected azimuth mis-registration. Note that for multilooked interferograms, as commonly used in geophysical applications, the impact of mis-registration will be much less, as shown in Fig. 20(c). This impact of mis-registration on the quality of the generated interferometric phase in a traditional range-Doppler grid (or radar coordinate system) also applies to the newly introduced concept of geocoded SLC [23], [24]. That is, if for any reason (e.g., the ionospheric range delay) the geocoded SLCs are not correctly aligned, the misaligned signals will interfere, resulting in the noisy interferogram similar to Fig. 20(a).

G. Geolocation Residuals at L-Band SAR

The residual range delay time series after bias corrections contains contributors from tectonic displacement [15], uncompensated tidal and loading effects (e.g., OTL, pole tides, and so on), orbital errors, and residual atmospheric delays due to the limited resolution of ERA5 and GIM products. The residual range delay of ALOS-2 is significantly larger than that of Sentinel-1 (0.56 versus 0.06 m; Fig. 19), the residual ionospheric delay is most likely the dominant source due to the following reasons.

1) The large magnitude of range delay (1 to 2 m) cannot be easily explained by the other possible sources, including the orbital error [54], but it can be explained with 4–8 TECU of residual ionospheric delay at the L-band which is in the order of GIM accuracy (4.5 TECU) [38] and of topside TEC magnitude.
2) The ratio of the ionospheric sensitivity between the L-band and the C-band SAR ($\sim$17) is about twice the ratio of range delay RMSE between ALOS-2 and Sentinel-1 stacks ($\sim$9), indicating an ionosphere-driven dispersive component in the L-band ALOS-2 residual and only part of the C-band Sentinel-1 residual.
3) The predicted range delay STD due to topside TEC for the L-band SAR (0.46 m in Chile; Section VII-C) is of similar magnitude as the observed range delay RMSE of ALOS-2 (0.56 m in Japan), indicating the observed residual range delay can be largely driven by the topside TEC.

This hypothesis cannot be easily evaluated, since there is no dual-frequency GNSS data available for ALOS-2 during SAR observation due to the interference of the radar frequency with the onboard GNSS L2 frequency [55], thereby inhibiting the

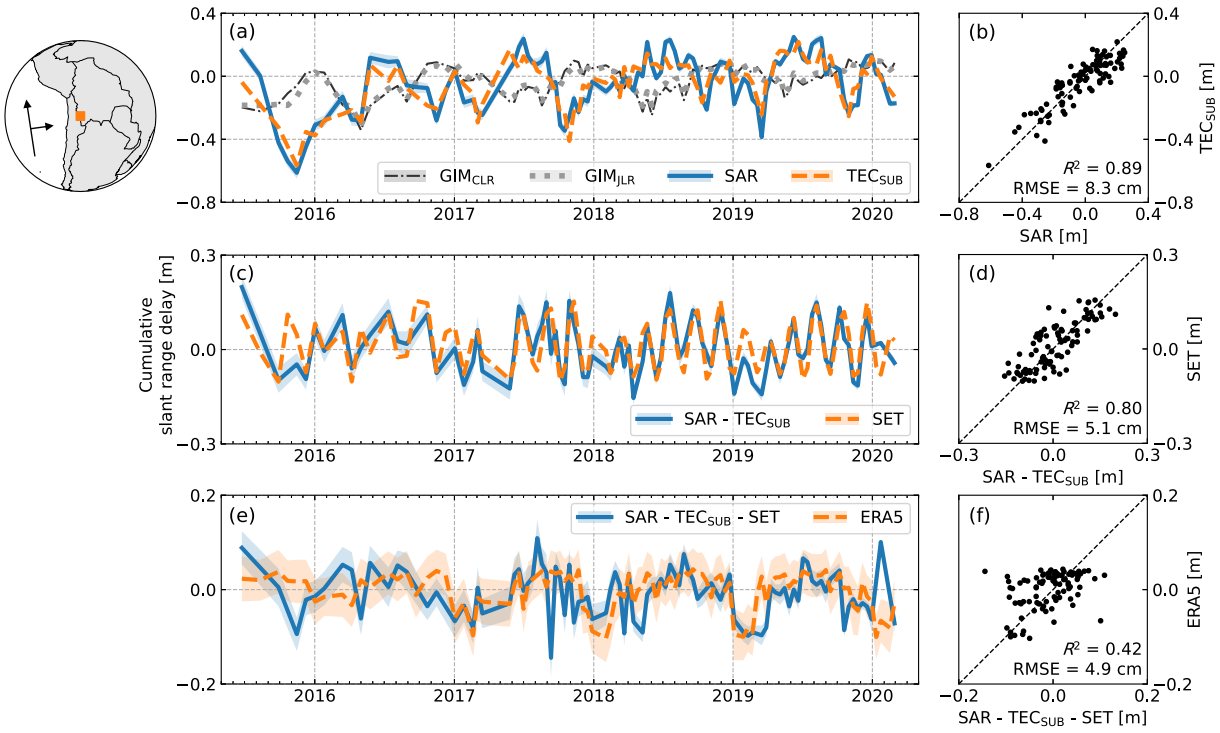

Fig. 21. Similar to Fig. 11, but corrected for the S1A/B range bias (Section VII-A) and the topside TEC (Section VII-C).

topside TEC estimation along the ALOS-2 orbit via the linear combination of the dual-frequency observations approach (Section IV-D).

H. Range Geolocation Error Budget for NISAR

We calculate the expected geolocation error budget in range direction for the upcoming NISAR mission based on existing literature. Assuming the uncertainties from the different sources of errors are uncorrelated, we derive the overall absolute and relative range geolocation accuracy after correcting for ionosphere using GIM, troposphere using ERA5 and SET in terms of bias ϵ and uncertainty σ as

$$\begin{cases} \epsilon = \epsilon_{\text{GIM}} + \epsilon_{\text{topTEC}} + \epsilon_{\text{tropo}} + \epsilon_{\text{tidal}} + \epsilon_{\text{orb}} + \epsilon_{\text{topo}} & (15) \\ \sigma = \sqrt{\sigma_{\text{GIM}}^2 + \sigma_{\text{topTEC}}^2 + \sigma_{\text{tropo}}^2 + \sigma_{\text{tidal}}^2 + \sigma_{\text{orb}}^2 + \sigma_{\text{topo}}^2} & (16) \end{cases}$$

where $\epsilon_{\text{GIM}} \pm \sigma_{\text{GIM}}$ represents the accuracy of GIM products and $\epsilon_{\text{topTEC}} \pm \sigma_{\text{topTEC}}$ represents the residual ionospheric contribution from ignoring the topside TEC [calculated via equation (6)–(11)]. The global accuracy of JLR GIM is 0.72 ± 4.49 TECU [38]. Although there is no study on the global accuracy of JHR GIM, our results over Chile and Japan demonstrated that JHR GIM is significantly more accurate than JLR GIM. Since northern Chile, located in the equatorial ionization anomaly crests, shows maximum topside TEC in the two snapshots during solar maximum and minimum [Fig. 9(a) and (b)], its statistics of the topside TEC of 6.6 ± 1.8 TECU (Section VII-C) can be considered as a conservative contribution of topside TEC to NISAR's range delay error budget. $\epsilon_{\text{tropo}} \pm \sigma_{\text{tropo}}$ represents the residual tropospheric delay after tropospheric correction using ERA5 with a bias up to 4 cm [56] and STD up to 5 cm [57] in the LOS direction. $\epsilon_{\text{tidal}} \pm \sigma_{\text{tidal}}$ represents the uncompensated periodic tidal effects, including the OTL, pole tides, and atmospheric loading with 0.0 ± 4.4 cm in the LOS direction (Section III-D). $\epsilon_{\text{orb}} \pm \sigma_{\text{orb}}$ represents the orbital error. We use Sentinel-1A as a proxy with an accuracy of 0.5 ± 3 cm [13]. $\epsilon_{\text{topo}} \pm \sigma_{\text{topo}}$ represents the contribution from DEM error. With an absolute vertical accuracy σ_z of 4 m in the global Copernicus DEM [58], we could calculate the resulting absolute and relative geolocation accuracy as [6], [59]

$$\begin{cases} \epsilon_{\text{topo}} = \sigma_z \cdot \cot(\theta) & (17) \\ \sigma_{\text{topo}} = \sigma_z \dfrac{B_\perp}{r \cdot \sin(\theta)} & (18) \end{cases}$$

where $B_\perp \leq 350$ m is perpendicular baseline [60].

Table IV summaries expected range geolocation accuracy for the NISAR L-band and S-band SAR. DEM error is the largest contributor to the absolute geolocation error but has a negligible impact on the relative geolocation accuracy. The ionosphere, especially the topside TEC, is the second-largest contributor to the absolute geolocation error and dominates the relative geolocation error. Note that this error budget represents an upper limit of the achievable geolocation accuracy in the range direction due to our limited knowledge of the global accuracy of JHR GIM and the global temporal and spatial variation of topside TEC.

VIII. Conclusion

We evaluate the range geolocation accuracy of the C- and L-band SAR with a focus on the ionospheric contribution and discuss methods to mitigate its impact. Ionospheric range delay is a nonlinear function of the vertical TEC. It dominates

the geolocation error for the C-band Sentinel-1 ascending (dusk side) orbit and the L-band ALOS-2 data. For Sentinel-1 descending (dawn side) orbit, solid Earth tides are the largest contributor. Comparisons between different GNSS-based TEC products show that the JPL high-resolution GIM (with 15-min temporal resolution and 1° spatial resolution) performs significantly better than the low-resolution GIM from JPL and CODE.

The topside ionosphere along Sentinel-1 orbits, sampled at two dates close to the latest solar maximum and minimum, demonstrate a global spatial variation of up to 12 TECU with a spatial pattern similar to the total TEC from GIM: higher TEC values at the equatorial ionization anomaly crests and polar regions than the mid-latitudes. A time series of topside TEC over a site in northern Chile demonstrate a temporal variation of 6.6 ± 1.8 TECU, which is equivalent to 1.7 ± 0.5 m of range delay in the L-band. Therefore, we conclude that the contribution of topside TEC to the geolocation error budget of the L-band SAR is significant and should be accounted for.

After correcting for ionosphere (using JHR GIM), troposphere (using ERA5), solid Earth tides, and S1A/B range bias for Sentinel-1, the RMSE of range mis-registration time series reduced from 0.20 to 0.06 m (and to 0.05 m with topside TEC) for Sentinel-1 and reduced from 2.66 to 0.56 m for ALOS-2 (with the maximum mis-registration reduced from 0.6 to 0.2 m for Sentinel-1 and reduced from 11.1 to 1.6 m for ALOS-2). For the C-band Sentinel-1, the geometrical coregistration with model-driven refinements is accurate enough in the range direction for most applications, including interferometry. For the L-band SAR, e.g., NISAR, the model-driven refinement could be potentially accurate enough in the range direction if topside TEC is available.

APPENDIX
MIS-REGISTRATION COMPARISON AFTER CORRECTING FOR S1A/B RANGE BIAS AND TOPSIDE TEC

Fig. 21 compares the estimated range mis-registration time series with the model predictions for Sentinel-1 ascending track 149 in Chile, after correcting for the S1A/B range bias (Section VII-A) and the topside TEC (Section VII-C).

DATA AVAILABILITY

The processed SAR offset and TEC data are available on Zenodo at https://doi.org/10.5281/zenodo.6360749.

CODE AVAILABILITY

The ionospheric mapping function is implemented in the MintPy software (https://github.com/insarlab/MintPy). The solid Earth tides code is wrapped as the PySolid package (https://github.com/insarlab/PySolid) under the GPLv3 license. Figures are plotted using Jupyter Notebook and available on GitHub (https://github.com/yunjunz/2022-Geolocation).

ACKNOWLEDGMENT

The Sentinel-1 data were provided by ESA and obtained from Alaska Satellite Facility. The ALOS-2 data were provided by JAXA. The DEM in Japan is provided by GSI. The authors would like to thank Lijun Zhu and Minyan Zhong for their development of PyCuAmpcor, Dennis Milbert for sharing the Fortran program for solid Earth tides calculation and discussion on the along-track time variation of SAR satellite, and Joseph Kennedy for the maintenance of PySolid. We would also like to thank Virginia Brancato, Scott Hensley, and Yujie Zheng for helpful discussions. The research was carried out partly at the Jet Propulsion Laboratory, California Institute of Technology, under a contract with the National Aeronautics and Space Administration.

REFERENCES

[1] B. Minchew, M. Simons, B. Riel, and P. Milillo, "Tidally induced variations in vertical and horizontal motion on Rutford Ice Stream, West Antarctica, inferred from remotely sensed observations," *J. Geophys. Res., Earth Surface*, vol. 122, no. 1, pp. 167–190, 2017, doi: 10.1002/2016JF003971.

[2] Y. Shao *et al.*, "Rice monitoring and production estimation using multitemporal RADARSAT," *Remote Sens. Environ.*, vol. 76, no. 3, pp. 310–325, Jun. 2001, doi: 10.1016/S0034-4257(00)00212-1.

[3] S.-H. Hong, S. Wdowinski, S.-W. Kim, and J.-S. Won, "Multitemporal monitoring of wetland water levels in the Florida Everglades using interferometric synthetic aperture radar (InSAR)," *Remote Sens. Environ.*, vol. 114, no. 11, pp. 2436–2447, Nov. 2010, doi: 10.1016/j.rse.2010.05.019.

[4] R. Jolivet, M. Simons, P. S. Agram, Z. Duputel, and Z. K. Shen, "Aseismic slip and seismogenic coupling along the central San Andreas fault," *Geophys. Res. Lett.*, vol. 42, no. 2, 2015, Art. no. 2014GL062222, doi: 10.1002/2014GL062222.

[5] Q. Lin, J. F. Vesecky, and H. A. Zebker, "New approaches in interferometric SAR data processing," *IEEE Trans. Geosci. Remote Sens.*, vol. 30, no. 3, pp. 560–567, May 1992, doi: 10.1109/36.142934.

[6] E. Sansosti, P. Berardino, M. Manunta, F. Serafino, and G. Fornaro, "Geometrical SAR image registration," *IEEE Trans. Geosci. Remote Sens.*, vol. 44, no. 10, pp. 2861–2870, Oct. 2006, doi: 10.1109/TGRS.2006.875787.

[7] J. C. Curlander, "Location of spaceborne SAR imagery," *IEEE Trans. Geosci. Remote Sens.*, vol. GE-20, no. 3, pp. 359–364, Jul. 1982, doi: 10.1109/TGRS.1982.350455.

[8] R. Michel, J.-P. Avouac, and J. Taboury, "Measuring near field coseismic displacements from SAR images: Application to the Landers earthquake," *Geophys. Res. Lett.*, vol. 26, no. 19, pp. 3017–3020, 1999, doi: 10.1029/1999GL900524.

[9] R. Scheiber and A. Moreira, "Coregistration of interferometric SAR images using spectral diversity," *IEEE Trans. Geosci. Remote Sens.*, vol. 38, no. 5, pp. 2179–2191, Sep. 2000, doi: 10.1109/36.868876.

[10] N. Yagüe-Martínez *et al.*, "Interferometric processing of Sentinel-1 TOPS data," *IEEE Trans. Geosci. Remote Sens.*, vol. 54, no. 4, pp. 2220–2234, Apr. 2016, doi: 10.1109/TGRS.2015.2497902.

[11] H. Fattahi, P. Agram, and M. Simons, "A network-based enhanced spectral diversity approach for TOPS time-series analysis," *IEEE Trans. Geosci. Remote Sens.*, vol. 55, no. 2, pp. 777–786, Feb. 2017, doi: 10.1109/TGRS.2016.2614925.

[12] H. Fattahi, M. Simons, and P. Agram, "InSAR time-series estimation of the ionospheric phase delay: An extension of the split range-spectrum technique," *IEEE Trans. Geosci. Remote Sens.*, vol. 55, no. 10, pp. 5984–5996, Oct. 2017, doi: 10.1109/TGRS.2017.2718566.

[13] H. Peter *et al.*, "Sentinel-1A–First precise orbit determination results," *Adv. Space Res.*, vol. 60, no. 5, pp. 879–892, 2017, doi: 10.1016/j.asr.2017.05.034.

[14] M. Eineder, C. Minet, P. Steigenberger, X. Cong, and T. Fritz, "Imaging geodesy—Toward centimeter-level ranging accuracy with TerraSAR-X," *IEEE Trans. Geosci. Remote Sens.*, vol. 49, no. 2, pp. 661–671, Feb. 2011, doi: 10.1109/TGRS.2010.2060264.

[15] X. Y. Cong, U. Balss, M. Eineder, and T. Fritz, "Imaging geodesy—Centimeter-level ranging accuracy with TerraSAR-X: An update," *IEEE Geosci. Remote Sens. Lett.*, vol. 9, no. 5, pp. 948–952, Sep. 2012, doi: 10.1109/LGRS.2012.2187042.

[16] C. Gisinger *et al.*, "In-depth verification of Sentinel-1 and TerraSAR-X geolocation accuracy using the Australian corner reflector array," *IEEE Trans. Geosci. Remote Sens.*, vol. 59, no. 2, pp. 1154–1181, Feb. 2021, doi: 10.1109/TGRS.2019.2961248.

[17] M. Eineder, "Efficient simulation of SAR interferograms of large areas and of rugged terrain," *IEEE Trans. Geosci. Remote Sens.*, vol. 41, no. 6, pp. 1415–1427, Jun. 2003, doi: 10.1109/TGRS.2003.811692.

[18] P. A. Rosen, E. Gurrola, G. F. Sacco, and H. Zebker, "The InSAR scientific computing environment," in *Proc. EUSAR*, Apr. 2012, pp. 730–733.

[19] P. A. Rosen, S. Hensley, G. Peltzer, and M. Simons, "Updated repeat orbit interferometry package released," *EOS, Trans. Amer. Geophys. Union*, vol. 85, no. 5, p. 47, 2004, doi: 10.1029/2004EO050004.

[20] D. Sandwell, R. Mellors, X. Tong, M. Wei, and P. Wessel, "Open radar interferometry software for mapping surface deformation," *EOS, Trans. Amer. Geophys. Union*, vol. 92, no. 28, p. 234, 2011, doi: 10.1029/2011EO280002.

[21] G. H. X. Shiroma, M. Lavalle, and S. M. Buckley, "An area-based projection algorithm for SAR radiometric terrain correction and geocoding," *IEEE Trans. Geosci. Remote Sens.*, vol. 60, pp. 1–23, 2022, doi: 10.1109/TGRS.2022.3147472.

[22] L. M. H. Ulander, H. Hellsten, and G. Stenström, "Synthetic-aperture radar processing using fast factorized back-projection," *IEEE Trans. Aerosp. Electron. Syst.*, vol. 39, no. 3, pp. 760–776, Jul. 2003, doi: 10.1109/TAES.2003.1238734.

[23] H. A. Zebker, "User-friendly InSAR data products: Fast and simple timeseries processing," *IEEE Geosci. Remote Sens. Lett.*, vol. 14, no. 11, pp. 2122–2126, Nov. 2017, doi: 10.1109/LGRS.2017.2753580.

[24] Y. Zheng and H. A. Zebker, "Phase correction of single-look complex radar images for user-friendly efficient interferogram formation," *IEEE J. Sel. Topics Appl. Earth Observ. Remote Sens.*, vol. 10, no. 6, pp. 2694–2701, Jun. 2017, doi: 10.1109/JSTARS.2017.2697861.

[25] J. Böhm and H. Schuh, *Atmospheric Effects in Space Geodesy*, vol. 5, 1st ed. Berlin, Germany: Springer-Verlag, 2013.

[26] A. El-Rabbany, *Introduction to GPS: The Global Positioning System*. Norwood, MA, USA: Artech House, 2002.

[27] H. Berrada Baby, P. Golé, and J. Lavergnat, "A model for the tropospheric excess path length of radio waves from surface meteorological measurements," *Radio Sci.*, vol. 23, no. 6, pp. 1023–1038, Nov. 1988, doi: 10.1029/RS023i006p01023.

[28] H. Hersbach *et al.*, "The ERA5 global reanalysis," *Quart. J. Roy. Meteorol. Soc.*, vol. 146, no. 730, pp. 1999–2049, Jun. 2020, doi: 10.1002/qj.3803.

[29] R. Jolivet, R. Grandin, C. Lasserre, M.-P. Doin, and G. Peltzer, "Systematic InSAR tropospheric phase delay corrections from global meteorological reanalysis data," *Geophys. Res. Lett.*, vol. 38, no. 17, Sep. 2011, Art. no. L17311, doi: 10.1029/2011GL048757.

[30] G. Petit and B. Luzum, "IERS conventions," International Earth Rotation And Reference Systems Service, IERS Technical Note 36, Frankfurt, Germany, Tech. Rep. 3-89888-989-6, 2010. [Online]. Available: http://www.iers.org/TN36/

[31] C. J. DiCaprio and M. Simons, "Importance of ocean tidal load corrections for differential InSAR," *Geophys. Res. Lett.*, vol. 35, no. 22, pp. 581–592, 2008, doi: 10.1029/2008GL035806.

[32] H. R. Martens, M. Simons, S. Owen, and L. Rivera, "Observations of ocean tidal load response in south America from subdaily GPS positions," *Geophys. J. Int.*, vol. 205, no. 3, pp. 1637–1664, Jun. 2016, doi: 10.1093/gji/ggw087.

[33] D. Dong, P. Fang, Y. Bock, M. K. Cheng, and S. Miyazaki, "Anatomy of apparent seasonal variations from GPS-derived site position time series," *J. Geophys. Res., Solid Earth*, vol. 107, no. B4, pp. ETG 9-1–ETG 9-16, Apr. 2002, doi: 10.1029/2001JB000573.

[34] P. Tregoning, C. Watson, G. Ramillien, H. McQueen, and J. Zhang, "Detecting hydrologic deformation using GRACE and GPS," *Geophys. Res. Lett.*, vol. 36, no. 15, p. L15401, Aug. 2009, doi: 10.1029/2009GL038718.

[35] D. Milbert. (2018). *Solid: Solid Earth Tide*. [Online]. Available: http://geodesyworld.github.io/SOFTS/solid.htm

[36] X. Xu and D. T. Sandwell, "Toward absolute phase change recovery with InSAR: Correcting for Earth tides and phase unwrapping ambiguities," *IEEE Trans. Geosci. Remote Sens.*, vol. 58, no. 1, pp. 726–733, Jan. 2020, doi: 10.1109/TGRS.2019.2940207.

[37] A. J. Mannucci, B. D. Wilson, D. N. Yuan, C. H. Ho, U. J. Lindqwister, and T. F. Runge, "A global mapping technique for GPS-derived ionospheric total electron content measurements," *Radio Sci.*, vol. 33, no. 3, pp. 565–582, 1998, doi: 10.1029/97RS02707.

[38] M. Hernàndez-Pajares *et al.*, "The IGS VTEC maps: A reliable source of ionospheric information since 1998," *J. Geodesy*, vol. 83, no. 3, pp. 263–275, Mar. 2009, doi: 10.1007/s00190-008-0266-1.

[39] J. Chen and H. A. Zebker, "Ionospheric artifacts in simultaneous L-band InSAR and GPS observations," *IEEE Trans. Geosci. Remote Sens.*, vol. 50, no. 4, pp. 1227–1239, Apr. 2012, doi: 10.1109/TGRS.2011.2164805.

[40] B. A. Iijima *et al.*, "Automated daily process for global ionospheric total electron content maps and satellite ocean altimeter ionospheric calibration based on global positioning system data," *J. Atmos. Sol.-Terr. Phys.*, vol. 61, no. 16, pp. 1205–1218, Nov. 1999, doi: 10.1016/S1364-6826(99)00067-X.

[41] S. Schaer, W. Gurtner, and J. Feltens, "IONEX: The ionosphere map exchange format version 1," in *Proc. IGS AC Workshop*, Darmstadt, Germany, vol. 9, 1998, pp. 1–12.

[42] X. Pi, A. J. Mannucci, and O. Verkhoglyadova, "Polar topside TEC enhancement revealed by Jason-2 measurements," *Earth Space Sci.*, vol. 8, no. 3, 2021, Art. no. e2020EA001429, doi: 10.1029/2020EA001429.

[43] NOAA Space Weather Prediction Center. (2019). *Solar Cycle 25 Forecast Update*. [Online]. Available: https://www.swpc.noaa.gov/news/solar-cycle-25-forecast-update

[44] A. Schaum and M. McHugh, "Analytic methods of image registration: Displacement estimation and resampling," Naval Res. Lab, Washington, DC, USA, Report NRL Rep. 9298, Feb. 1991. [Online]. Available: https://apps.dtic.mil/sti/pdfs/ADA233385.pdf

[45] P. Berardino, G. Fornaro, R. Lanari, and E. Sansosti, "A new algorithm for surface deformation monitoring based on small baseline differential SAR interferograms," *IEEE Trans. Geosci. Remote Sens.*, vol. 40, no. 11, pp. 2375–2383, Nov. 2002, doi: 10.1109/TGRS.2002.803792.

[46] F. Casu, A. Manconi, A. Pepe, and R. Lanari, "Deformation time-series generation in areas characterized by large displacement dynamics: The SAR amplitude pixel-offset SBAS technique," *IEEE Trans. Geosci. Remote Sens.*, vol. 49, no. 7, pp. 2752–2763, Jul. 2011, doi: 10.1109/TGRS.2010.2104325.

[47] S.-H. Yun, H. Zebker, P. Segall, A. Hooper, and M. Poland, "Interferogram formation in the presence of complex and large deformation," *Geophys. Res. Lett.*, vol. 34, no. 12, p. L12305, 2007, doi: 10.1029/2007GL029745.

[48] Z. Yunjun, H. Fattahi, and F. Amelung, "Small baseline InSAR time series analysis: Unwrapping error correction and noise reduction," *Comput. Geosci.*, vol. 133, Dec. 2019, Art. no. 104331, doi: 10.1016/j.cageo.2019.104331.

[49] Z. Yunjun, F. Amelung, and Y. Aoki, "Imaging the hydrothermal system of Kirishima volcanic complex with L-band InSAR time series," *Geophys. Res. Lett.*, vol. 48, no. 11, 2021, Art. no. e2021GL092879, doi: 10.1029/2021GL092879.

[50] T. G. Farr *et al.*, "The shuttle radar topography mission," *Rev. Geophys.*, vol. 45, no. 2, p. RG2004, 2007, doi: 10.1029/2005RG000183.

[51] C. Liang, P. Agram, M. Simons, and E. J. Fielding, "Ionospheric correction of InSAR time series analysis of C-band Sentinel-1 TOPS data," *IEEE Trans. Geosci. Remote Sens.*, vol. 57, no. 9, pp. 6755–6773, Sep. 2019, doi: 10.1109/TGRS.2019.2908494.

[52] A. Solgaard *et al.*, "Greenland ice velocity maps from the PROMICE project," *Earth Syst. Sci. Data*, vol. 13, no. 7, pp. 3491–3512, Jul. 2021, doi: 10.5194/essd-13-3491-2021.

[53] H. Hofmann, H. Wickham, and K. Kafadar, "Letter-value plots: Boxplots for large data," *J. Comput. Graph. Statist.*, vol. 26, no. 3, pp. 469–477, 2017, doi: 10.1080/10618600.2017.1305277.

[54] K. Akiyama, H. Itoh, H. Masuda, S. Kasho, and T. Sakamoto, "Operational validation of precise orbit determination for ALOS-2," in *Proc. 14th Int. Conf. Space Oper.*, 2016, pp. 1–14, doi: 10.2514/6.2016-2521.

[55] Y. Arikawa, Y. Osawa, Y. Hatooka, S. Suzuki, and Y. Kankaku, "Development status of Japanese advanced land observing satellite-2," *Proc. SPIE*, vol. 7826, Oct. 2010, Art. no. 78260B, doi: 10.1117/12.866675.

[56] C. Yu, Z. Li, and G. Blewitt, "Global comparisons of ERA5 and the operational HRES tropospheric delay and water vapor products with GPS and MODIS," *Earth Space Sci.*, vol. 8, no. 5, May 2021, Art. no. e2020EA001417, doi: 10.1117/12.866675.

[57] H. Fattahi and F. Amelung, "InSAR bias and uncertainty due to the systematic and stochastic tropospheric delay," *J. Geophys. Res., Solid Earth*, vol. 120, no. 12, pp. 8758–8773, 2015, doi: 10.1002/2015JB012419.

[58] E. Fahrland, P. Jacob, H. Schrader, and H. Kahabka. (2020). *Copernicus Digital Elevation Model Product Handbook*. [Online]. Available: https://spacedata.copernicus.eu/documents/20126/0/GEO1988-CopernicusDEM-SPE-002_ProductHandbook_I3.0.pdf

[59] J. Jung, D.-J. Kim, S. K. Palanisamy Vadivel, and S.-H. Yun, "Long-term deflection monitoring for bridges using X and C-band time-series SAR interferometry," *Remote Sens.*, vol. 11, no. 11, p. 1258, May 2019.

[60] NISAR, "NASA-ISRO SAR (NISAR) mission science users' handbook," NASA Jet Propuls. Lab., Pasadena, CA, USA, Tech. Rep. 18-1893, 2018. [Online]. Available: https://nisar.jpl.nasa.gov/system/documents/files/26_NISAR_FINAL_9-6-19.pdf

Zhang Yunjun received the B.Eng. degree in remote sensing from the Wuhan University, Wuhan, China, in 2011, the M.Sc. degree in geodesy from the University of Chinese Academy of Sciences, Beijing, China, in 2014, and the Ph.D. degree in geophysics from the University of Miami, Miami, FL, USA, in 2019.

He has been a Post-Doctoral Scholar Research Associate with the Seismological Laboratory, Division of Geological and Planetary Sciences, California Institute of Technology, Pasadena, CA, USA, since 2019. His research interests include algorithm and tools development for interferometric synthetic aperture radar time series analysis and solid Earth processes associated with active volcanism and tectonics.

Heresh Fattahi (Member, IEEE) received the B.Sc. degree in geomatics engineering from Isfahan University, Isfahan, Iran, in 2004, the M.Sc. degree in remote sensing engineering from the K. N. Toosi University of Technology, Tehran, Iran, in 2007, and the Ph.D. degree in geophysics from the University of Miami, Miami, FL, USA, in 2015.

He was a Post-Doctoral Scholar with the Seismological Laboratory, California Institute of Technology, Pasadena, CA, USA, from 2015 to 2017. He joined the SAR Algorithms and Processing Group, Radar Science and Engineering Section, Jet Propulsion Laboratory, as a Signal Analysis Engineer, in 2017, is currently leading the level-2 product development for NASA–ISRO synthetic aperture radar (NISAR) mission and the algorithm development team for Observational Products for End-users using Remote sensing Analysis (OPERA). His research interests include algorithm development for SAR, interferometric SAR (InSAR), and InSAR time series analysis, with emphasis on error analysis and uncertainty quantification, big-data analysis, and analysis-ready products generation for science and application users.

Xiaoqing Pi received the B.S. degree in radio wave propagation and antenna and the M.S. degree in space physics from Wuhan University, Wuhan, China, in 1982 and 1985, respectively, and the Ph.D. degree in astronomy from Boston University, Boston, MA, USA, in 1995.

He joined NASA's Jet Propulsion Laboratory, California Institute of Technology, Pasadena, CA, USA, in 1996. He has conducted a variety of developments for measuring and modeling the ionosphere, including global maps of ionospheric irregularities (GMIIS), global assimilative ionospheric model (GAIM), ionospheric multimodel ensemble prediction system, the rate of TEC index and small-scale TEC slopes, combined global TEC gradients, plasmaspheric measurements from low Earth orbiters, and machine-learning prediction of regional ionospheric irregularities and scintillation. His research interests include ionospheric remote sensing and modeling, coupling of magnetosphere–ionosphere–thermosphere, and ionospheric effects of space weather.

Paul Rosen (Fellow, IEEE) received the B.S. and M.S. degrees from the University of Pennsylvania, Philadelphia, PA, USA, in 1981 and 1982, respectively, and the Ph.D. degree from Stanford University, Stanford, CA, USA, in 1990, all in electrical engineering.

He is currently the Project Scientist for NASA–ISRO synthetic aperture radar (NISAR) mission at the Jet Propulsion Laboratory (JPL), California Institute of Technology, Pasadena, CA, where he is also a Visiting Faculty Member with the Division of Geological and Planetary Sciences. He is also the Study Coordinator for NASA's Surface Deformation and Change Decadal Survey Architecture Study. His assignments at JPL have encompassed scientific and engineering research and development of radar instruments and applications, and technical, organizational, and programmatic management of radar developments at JPL. He has authored over 40 journal and book chapter publications and over 100 conference papers.

Dr. Rosen currently serves as the IEEE Geoscience and Remote Sensing Society Director for Global Activities.

Mark Simons (Senior Member, IEEE) received the B.Sc. degree in geophysics and space physics from the University of California at Los Angeles, Los Angeles, CA, USA, in 1989, and the Ph.D. degree in geophysics from the Massachusetts Institute of Technology, Cambridge, MA, USA, in 1996.

He has been with the California Institute of Technology, Pasadena, CA, since 1996, where he is the John W. and Herberta M. Miles Professor of geophysics with the Seismological Laboratory, Division of Geological and Planetary Sciences. He is also the Chief Scientist of the Jet Propulsion Laboratory, Pasadena. His research interests include processes associated with the seismic cycle, migration of magma and water in the subsurface, tides, and glacial rebound, tectonics and the relationship between short and long time-scale processes, glaciology, with an emphasis on basal mechanics and ice rheology, tools and applications using space geodesy, with emphasis on global navigation satellite system and synthetic aperture radar, Bayesian methods for large geophysical inverse problems, and applications of space geodesy for monitoring and rapid response to natural disasters.

Dr. Simons is a fellow of the American Geophysical Union.

Piyush Agram received the B.Tech. degree in electrical engineering from the Indian Institute of Technology Madras, Chennai, India, in 2004, and the Ph.D. degree in electrical engineering from Stanford University, Stanford, CA, USA, in 2010.

He was with the Seismological Laboratory and the Keck Institute of Space Studies, California Institute of Technology, Pasadena, CA, as a Post-Doctoral Scholar until 2013. He was a member of the Radar Algorithms and Processing Group, Jet Propulsion Laboratory, Pasadena, from 2013 to 2020. His research interests include algorithm development for synthetic aperture radar interferometry, deformation time series applications, and geospatial big data analysis.

Yosuke Aoki (Member, IEEE) received the B.S., M.S., and Ph.D. degrees from the Department of Earth and Planetary Science, The University of Tokyo, Tokyo, Japan, in 1996, 1998, and 2001.

He was a Lamont Post-Doctoral Fellow with the Lamont–Doherty Earth Observatory, Columbia University, New York, NY, USA, between 2001 and 2003. He was an Assistant Professor with the Earthquake Research Institute, The University of Tokyo, between 2003 and 2019, where he is currently an Associate Professor and an Adjunct Professor with the Department of Earth and Planetary Science. He is also a Visiting Scientist with the RIKEN Center for Advanced Photonics, Tokyo. His research interests include measuring Earth's deformation with space geodetic techniques, such as synthetic aperture radar and global navigation satellite systems, and developing physical models to explain the observed surface deformation.